



Surface cholesterol-enriched domains specifically promote invasion of breast cancer cell lines by controlling invadopodia and extracellular matrix degradation

Mauriane Maja¹ · Danahe Mohammed² · Andra C. Dumitru² · Sandrine Verstraeten³ · Maxime Lingurski¹ · Marie-Paule Mingeot-Leclercq³ · David Alsteens² · Donatienne Tyteca¹

Received: 16 March 2022 / Revised: 7 June 2022 / Accepted: 13 June 2022 / Published online: 12 July 2022
© The Author(s) 2022

Abstract

Tumor cells exhibit altered cholesterol content. However, cholesterol structural subcellular distribution and implication in cancer cell invasion are poorly understood mainly due to difficulties to investigate cholesterol both quantitatively and qualitatively and to compare isogenic cell models. Here, using the MCF10A cell line series (non-tumorigenic MCF10A, pre-malignant MCF10AT and malignant MCF10CA1a cells) as a model of breast cancer progression and the highly invasive MDA-MB-231 cell line which exhibits the common TP53 mutation, we investigated if cholesterol contributes to cancer cell invasion, whether the effects are specific to cancer cells and the underlying mechanism. We found that partial membrane cholesterol depletion specifically and reversibly decreased invasion of the malignant cell lines. Those cells exhibited dorsal surface cholesterol-enriched submicrometric domains and narrow ER-plasma membrane and ER-intracellular organelles contact sites. Dorsal cholesterol-enriched domains can be endocytosed and reach the cell ventral face where they were involved in invadopodia formation and extracellular matrix degradation. In contrast, non-malignant cells showed low cell invasion, low surface cholesterol exposure and cholesterol-dependent focal adhesions. The differential cholesterol distribution and role in breast cancer cell invasion provide new clues for the understanding of the molecular events underlying cellular mechanisms in breast cancer.

Keywords Matrigel invasion · Cholesterol transversal asymmetry · Endocytosis · Membrane contact sites · MCF10A series · MDA-MB-231

Abbreviations

A	MCF10A
AT	MCF10AT
AFM	Atomic force microscopy
CA1a	MCF10CA1a
chol	Cholesterol
cytoD	Cytochalasin D
ER	Endoplasmic reticulum

ECM	Extracellular matrix
MMP	Matrix metalloproteinase
mβCD	Methyl-β-cyclodextrin
PC	Phosphatidylcholine
PE	Phosphatidylethanolamine
PM	Plasma membrane
PS	Phosphatidylserine
SM	Sphingomyelin

✉ Donatienne Tyteca
donatienne.tyteca@uclouvain.be

¹ CELL Unit and PICT Imaging Platform, de Duve Institute, UCLouvain, B1.75.05, avenue Hippocrate, 75, 1200 Brussels, Belgium

² Louvain Institute of Biomolecular Science and Technology (LIBST), UCLouvain, Ottignies-Louvain-la-Neuve, Belgium

³ Cellular and Molecular Pharmacology Unit (FACM), Louvain Drug Research Institute, UCLouvain, Brussels, Belgium

Introduction

Cell migration is a fundamental property of cancer and metastasis. Formation and growth of secondary tumor require cancer cells to navigate through diverse microenvironments, including extracellular matrix (ECM) and blood vessels, and to adapt to mechanical stresses applied to them. Cancer cell lines and cells derived from cancerous tissues exhibit an increased deformability as compared

to their healthy counterparts [1–4]. Cancer cells are able to adapt their morphology and invasiveness by remodeling their cytoskeleton in connection with their nanomechanical properties [5]. However, the contribution of the plasma membrane (PM) lipid content and biophysical properties in cancer cell invasion is poorly understood [6, 7].

Due to aberrant lipid metabolism, cancer cells exhibit an altered PM lipid profile as compared to their healthy counterparts [6]. Although some common features can be highlighted, including ceramide loss and phosphatidylserine (PS) surface exposure [8–12], membrane lipid alterations are generally tumor-specific and even subtype-specific. For instance, the human MT3 breast cancer cell line exhibits an increase in mono- and polyunsaturated fatty acid content which correlates with metastasis [13]. Lipidomic analyses of the highly invasive MDA-MB-231 cell line have shown that PS, phosphatidylglycerol and phosphatidic acid are upregulated while sphingomyelin (SM) is downregulated as compared to the poorly invasive MCF7 cell line [14]. In contrast, using the MCF10A cell line series, Vidavsky et al. evidenced that SM is increased while phosphatidylethanolamine (PE) and phosphatidylcholine (PC) are less abundant in invasive cells compared to precancerous cultures [15]. In breast cancer samples, the absence of estrogen receptors is associated with upregulated SM, PC, PE and phosphatidylinositol species and specific PC species correlate with more aggressive breast tumors and poorer overall survival [16].

Cholesterol (chol) content is also generally described as altered in breast cancer. For instance, higher expression of chol biosynthesis genes has been shown to associate with a worse prognosis of basal-like breast cancer patients [17]. Multidrug-resistant cells exhibit higher chol that turns the PM more rigid and, thus, less permeable for drugs [18]. On the other hand, lower chol levels in metastatic cells correlate with a more deformable PM, increasing its invading capacity [13, 19]. Nevertheless, it is not known whether PM chol distribution is also deregulated in breast cancer and how. The difficulties could result from the lack of appropriate chol visualization tools and of high-resolution live microscopy approaches requested to analyze lipids, but also from the limited availability of isogenic cell models to evaluate the specificity of the effects. We recently used atomic force microscopy (AFM) combined with chol vital imaging by the domain 4 (D4) of the bacterial toxin perfringolysin O coupled to mCherry (hereafter named Theta toxin fragment [20–22]) on the MCF10A cell line series [23]. This model includes three human mammary cell lines, which offer the same background but increasing degrees of malignancy: MCF10A (A, non-tumorigenic), MCF10AT (AT, pre-malignant) and MCF10CA1a (CA1a, malignant) [24]. We showed that, while the cytoskeleton of the malignant CA1a cell line is, as expected, softer than normal A cells, its PM

is surprisingly stiffer and correlates with higher surface chol content and cell malignancy [23].

In the present study, we used the same series of breast cell lines to investigate (1) if surface chol contributes to cancer cell invasion, (2) whether the effects are specific to cancer cells, opening the possibility to specifically target this lipid in cancer, and (3) the underlying mechanism. To then test for the relevance of our observations, the study was extended to the triple-negative breast cancer cell line, MDA-MB-231, which exhibits the common TP53 mutation and is highly invasive [25]. We showed that the surface chol was specifically required for invasion of malignant CA1a and MDA-MB-231 cells. This surface chol was distributed in submicrometric domains that can be endocytosed and reach the cell ventral face where they were involved in the formation of invadopodia, allowing for gelatin degradation. Our data help to better understand the contribution of membrane chol to breast cancer cell invasion.

Materials and methods

Antibodies and reagents

Rabbit anti-Vimentin (D21H3, immunofluorescence IF 1:100, western blotting WB 1:100) and rabbit anti-Cortactin (H222, IF 1:200, WB 1:1000) were from Cell Signaling Technology. Mouse anti-Paxillin (5H11, IF 1:200, WB 1:1000) and TopFluor[®] Cholesterol (810255P) were from Merck Millipore. Mouse anti-KDEL (10C3, IF 1:300), Dyngo[®] 4a (ab120689) and Hoechst 33258 (ab228550) were from Abcam. Alexa Fluor[™] 568 Phalloidin (A12380), Alexa Fluor[™] 647 Phalloidin (A22287), Oregon Green[™] 488 conjugate (G13186), Fluo4-AM (F-14201), ER-Tracker[™] Red (E34250), LysoTracker[™] Green DND-26 (L7526), LysoTracker[™] Red DND-99 (L7528), Alexa Fluor 568 Transferrin (T23365), DAPI (D3571) and fluorescent secondary antibodies were from ThermoFisher Scientific. Peroxidase-conjugated secondary antibodies were from ThermoFisher Scientific and Sigma. SiR-actin (SC001) was from Spirochrome. GM6001 MMP inhibitor (BML-EI300-0001) was from Enzo Life Sciences. Mouse anti- α -Tubulin (DM1a, IF 1:100, WB 1:1000), methyl- β -cyclodextrin (m β CD; C4555), cholesterol-Water Soluble (C4951), cytochalasin D (cytoD) from Zygosporium mansonii (C8273) and growth factor-reduced ECM gel from Engelbreth-Holm-Swarm mouse sarcoma (E6909) were from Sigma-Aldrich.

Expression and purification of Theta toxin fragment

The expression plasmid pET28/His-mCherry-Theta-D4 encodes for an N-terminal 6xHis-tag followed by the monomeric red fluorescent protein mCherry and the C-terminal

non-toxic domain D4 of the chol-specific Theta toxin (Theta-D4). The plasmid was generated by swapping Dronpa for mCherry from pET28/His-Dronpa-theta-D4 [26]. Expression, purification, biochemical characterization and storage of Theta toxin fragment were performed as described in [20].

Cell line culture and chemical treatments

MCF10A, AT and CA1a cell lines were grown as previously described with the addition of 10 mM Hepes in the media [23]. MDA-MB-231 were grown in DMEM supplemented with 10% Fetal Bovine Serum (FBS), penicillin (100 U mL⁻¹) and streptomycin (100 µg mL⁻¹) at 37 °C with 5% CO₂. To partially deplete chol, cells were pre-incubated in a serum-free medium containing 1–6 mM mβCD for 2 h at 37 °C. To replete chol, depleted cells were subsequently incubated in serum-free medium containing mβCD charged with chol in a (6:1) molar ratio for 1 h. To inhibit MMP activity, cells were maintained during the whole experiment in a serum-free medium containing 10 µM GM6001 at 37 °C. To inhibit actin polymerization, cells were pre-incubated in a serum-free medium containing 0.5 µM cytoD for 2 h at 37 °C. To inhibit endocytosis, cells were preincubated in a serum-free medium containing 20 µM Dyngo4a for 30 min at 37 °C. The drug was maintained during the whole experiment. To check for the efficiency of mβCD and maintenance of effect during the time needed for an invasion assay despite agent removal, the total cell chol content was extracted and assessed with an Amplex Red cholesterol assay kit (Invitrogen) exactly as previously described [23].

Matrigel invasion assay

ECM Gel was diluted in DMEM to a final concentration of 0.5 or 2 mg mL⁻¹. 140 µL were then added to the ThinCert™ Tissue Culture Inserts (8 µm pore size, Greiner) and allowed to polymerize overnight at 37 °C. Excess of ECM Gel was removed by vacuum and 3.5 × 10⁴ cells were seeded on top of the ECM Gel-coated insert and allowed to adhere overnight. Cells were either serum-starved or pre-treated with 2 mM mβCD in combination or not with 0.5 µM cytoD for 2 h. Alternatively, they were repleted with chol for 1 h. Bottom chamber was filled with serum-free medium (background control) or 10% serum-containing medium (to assess total invasion) and cells were allowed to invade the ECM Gel for 6–12 h or 24 h. For the latter condition, cell proliferation was inhibited by 30 µM Mitomycin C (Sigma). Invading cells were fixed in 4% paraformaldehyde (PAF) for 20 min, stained with crystal violet for 10 min and washed with phosphate buffer saline (PBS). Non-invading cells were wiped from the upper chamber with a cotton swab. Ten images per insert were captured with a wide-field fluorescence microscope Observer.Z1 (20× objective). To quantify

the number of invading cells per condition, the total area of invading cells was determined by the ZEN 2.6 software (Blue edition, Zeiss) and was then divided by the area of a single cell manually surrounded. The invasion was calculated by subtracting the background control from the total number of invading cells.

AFM Young's Modulus measurements and data analysis

AFM images were acquired using an atomic force microscope (Bioscope Resolve, Bruker) operated in the PeakForce QNM mode (Nanoscope software v9.2) and coupled to an inverted epifluorescence microscope (Zeiss Observer Z.1). A 40× oil objective (NA = 0.95) was used. The AFM was equipped with a 150 µm piezoelectric scanner and a cell-culture chamber allowing to control the temperature, the humidity and the CO₂ concentration [27]. Overview images of cell surfaces (~30 µm²) were recorded at imaging forces of 500 pN using PFQNM-LC probes (Bruker) having tip lengths of 17 µm, tip radii of 65 nm and opening angles of 15°. The spring constant of the cantilevers was calibrated with a vibrometer (OFV-551 Polytec, Waldbronn) by the manufacturer. The pre-calibrated spring constant was used to determine the deflection sensitivity using the thermal noise method before each experiment [28]. The AFM tip was oscillated in a sinusoidal fashion at 0.25 kHz with a 750 nm amplitude in the PeakForce Tapping mode. The sample was scanned using a frequency of 0.2 Hz and 128 pixels per line. AFM images were analyzed and Young's modulus values of elasticity were extracted as previously described [23].

Live cell imaging of cholesterol, actin, calcium, endoplasmic reticulum, lysosomes and transferrin and quantification of surface cholesterol

Coverslips were coated with 20 µg mL⁻¹ fibronectin (Sigma-Aldrich) overnight at 4 °C or left uncoated. Cells were grown on coverslips overnight, washed 2 times with DMEM/F12 at room temperature and then labeled. For chol labeling, cells were incubated with 1.5 µM mCherry-Theta toxin fragment in fatty acid-free Bovine Serum Albumin (1 mg mL⁻¹) for 20 min at the indicated temperature, as previously described [20], or incubated in serum-free medium containing 15 µM mβCD charged with 5 µM TopFluor-Cholesterol in a (3:1) molar ratio for 20 min at 4 °C. For actin labeling, cells were incubated with 1 µM SiR-actin probe for 25 min at 37 °C. For calcium (Ca²⁺) labeling, cells were incubated with 1 µM Fluo4-acetoxymethyl (AM) ester for 1 h at 37 °C then incubated in serum-free medium for a further 30 min at 37 °C to allow for de-esterification of AM esters. For ER and lysosomes labeling, cells were respectively incubated with 1 µM ER-Tracker and 50–100 nM LysoTracker probe

for 30 min at 37 °C. The latter probe was maintained during the whole experiment, including the washing step. For fluorescent Transferrin endocytosis tracking, cells were incubated with 20 µg mL⁻¹ Alexa 568-transferrin for 10 min at 37 °C. Labeled cells were then washed 2 times with DMEM/F12 at room temperature. Coverslips with labeled living cells were placed in medium-filled LabTek chambers and observed with a Zeiss Cell Observer Spinning Disk (COSD) confocal microscope using a plan-Apochromat 63×NA 1.4 water immersion objective. X–Y confocal images and/or z-stacks were taken. Chol distribution at the top of the cells was quantified on z-stacks using ImageJ/Fiji. Images were converted to 8-bit grayscale and the mean grey value of the background was subtracted from the mean grey value of Theta fluorescence at the top section of each cell. Data are presented as Theta dorsal fluorescence intensity.

Cell immunofluorescence and quantification of focal adhesions, invadopodia, endoplasmic reticulum spreading, ER-Lysosomes contacts and apoptosis

Cells were seeded on glass or fibronectin-coated coverslips, washed with PBS, fixed with 4% PAF for 30 min, washed with PBS 5 times for 5 min, permeabilized with 0.1% Triton X-100 in PBS for 15 min and blocked with 5% Normal Goat Serum in PBS for 1 h, all at room temperature. Fixed cells were then immunolabeled with primary antibodies overnight at 4 °C, washed with PBS 3 times for 5 min, stained with fluorescent secondary antibody or Alexa Fluor™ Phalloidin and Hoechst 33258 for 1 h or DAPI for 5 min at room temperature in the dark, washed again with PBS 3 times for 5 min, mounted with Dako and examined with the COSD confocal microscope using a plan-Apochromat 100×NA 1.4 oil immersion objective and the same settings for illumination. Quantification of focal adhesions number and size was done using ImageJ/Fiji [29]. In brief, confocal images were opened in grayscale (black and white) mode, the background was subtracted using a rolling ball algorithm, local contrast of the images was enhanced by running CLAHE (Contrast Limited Adaptive Histogram Equalization) plugin, background was further minimized by applying mathematical exponential (EXP) and a manual threshold was used to segment areas of focal adhesions based on areas positive for paxillin. Number of cells presenting focal adhesions was counted manually based on paxillin and Hoechst nuclear staining. For invadopodia, the brightness and contrast of confocal images were adjusted manually to visualize invadopodia double positive for actin and cortactin and the area of invadopodia was manually surrounded by the generated images. Number of cells presenting invadopodia was counted manually based on actin, cortactin and Hoechst nuclear staining. Quantification of ER spreading through the cytoplasm was done using ImageJ/Fiji. Images were converted to 8-bit grayscale and manual threshold was used to segment areas of

ER and cytoplasm based on KDEL and α-Tubulin labeling, respectively. Data are presented as difference between cytoplasm and ER areas. Contacts between LysoTracker⁺ structures and ER were quantified based on fluorescence intensity profiles. Each peak of LysoTracker signal was assigned a score of 0 or 1 (0 = no contact with ER signal peak; 1 = close contact with ER signal peak). Data are expressed as a percentage of close contacts between LysoTracker⁺ structures and ER on total LysoTracker⁺ structures. For apoptosis, number of apoptotic nuclei was counted manually based on morphology and DAPI staining and expressed in percentage of total nuclei.

Gelatin degradation assay and quantification

Oregon Green™ 488 conjugate gelatin-coated coverslips were prepared as previously described [30]. Coverslips were equilibrated in serum-containing medium for 1 h at 37 °C before plating 1 × 10⁵ cells per coverslip. Cells were starved or treated for 2 h before incubation in serum-containing medium for 6–12 h to allow gelatin matrix degradation. Immunofluorescence staining was performed as described above and immunolabeled cells were examined with the COSD confocal microscope using a plan-Apochromat 63×NA 1.4 water immersion objective and the same settings for illumination. Quantification of total gelatin degradation area per total cell area was done using ImageJ/Fiji [30]. In brief, confocal images were opened in grayscale (black and white) mode, background was subtracted using a rolling ball algorithm and manual threshold was used to segment areas of gelatin degradation based on black areas in the Oregon Green fluorescent gelatin vs total cell area based on Phalloidin labeling. Data are presented as total gelatin degradation area per total cell area.

Statistical analyses

Statistical analyses were performed using GraphPad Prism Version 8.0.2. All data are expressed as means of *n* independent experiments ± SD. Statistical tests were performed only when *n* ≥ 3. Tests were non-parametrical when *n* ≤ 10. To compare the three cell lines and the effect of multiple treatments, parametrical ordinary one-way ANOVA followed by a suitable post-hoc comparison test or non-parametrical Kruskal–Wallis test followed by Dunn's comparison test were performed. To compare two samples, parametrical unpaired t test or non-parametrical unpaired Mann–Whitney test were done. To compare the effect of one treatment with a hypothetical mean of 100% representing the control, parametrical one-sample t test or non-parametrical Wilcoxon signed-rank test were performed. Comparisons between two or more groups are indicated with bars on top of the graphs. Comparisons with the control value are indicated above the columns. ns not significant, **p* < 0.05, ***p* < 0.01, ****p* < 0.001, *****p* < 0.0001.

Results

The higher invasion potential of malignant cells specifically depends on matrix metalloproteinase activity and cholesterol content

To determine the invasion potential of the three MCF10A cell lines, we used Transwells coated with Matrigel in the presence of 10% serum gradient in the bottom well. Modulation of confinement (through 0.5 mg mL⁻¹-loose and 2 mg mL⁻¹-dense Matrigel layers) and time of invasion (6, 12 and 24 h) revealed that low confinement favored the pre-malignant AT cell invasion while high confinement was needed to increase malignant CA1a cell invasion, no matter the time of the assay (Fig. S1, Fig. 1A, B). We, therefore, chose a 12 h invasion assay in a dense 2 mg mL⁻¹ Matrigel layer to better discriminate the three cell lines for their invasion. Upon global inhibition of extracellular matrix metalloproteinases (MMP) activity with GM6001, the malignant cell invasion was specifically decreased (Fig. 1C).

We then asked whether the differential extent of invasion of the three cell lines could be related to their differential cytocortex and PM stiffness as well as their distinct chol content and surface distribution [23]. Cell invasion seemed to inversely associate with the extent of cytocortex stiffness and total chol content but positively with the extent of PM stiffness and surface chol content (compare Fig. 1A, B with Fig. S2). Since chol is a key regulator of PM properties including stiffness [18, 31, 32], we further investigated the specific dependence of the malignant cells to this lipid for invasion. The membrane chol content was depleted by a 2 h incubation with 2 mM methyl- β -cyclodextrin (m β CD). This treatment was not cytotoxic and was specific towards chol as revealed by thin layer chromatography (Fig. S3). The ~30–45% depletion obtained, which was maintained after 12 h incubation in an m β CD-free medium, induced a specific decrease of CA1a cell invasion (Fig. 1D, E). Invasion and residual chol content were very well correlated (Fig. 1F), which was confirmed upon incubation of CA1a cells with increasing concentrations of m β CD (Fig. 1G–I). Altogether, the differential extent of invasion of the pre-malignant vs malignant cells suggested a distinct mode of invasion compatible with the specific dependence of the malignant cells on MMP activity and chol content.

The surface cholesterol of malignant cells is distributed in submicrometric domains that can be specifically and reversibly decreased by cholesterol depletion

To explore the mechanism behind the chol-dependent invasion of the malignant cells, we first evaluated the chol

surface distribution by cell labeling at 4 °C with the chol-specific mCherry-Theta toxin which specifically binds to chol and allowed us to reveal chol-enriched domains on living red blood cells ([20]; Fig. S4). The signal at the dorsal surface was then quantified on X–Z reconstructions. The chol surface content was higher in malignant CA1a cells, was distributed into submicrometric domains and was decreased upon m β CD (Fig. 2A, B). Such distribution agreed with our previous data obtained by AFM using Theta toxin derivatized tips which allowed to evidence chol-enriched domains in a label-free manner with high spatial resolution [23]. In addition, it was confirmed by PM insertion of the fluorescent chol analog TopFluor-Chol [33–35]. Thus, X–Z reconstructions and profiles revealed a heterogeneous distribution in clusters similar in size and m β CD sensitivity to those observed upon Theta labeling (Fig. S5A, B). Moreover, TopFluor-Chol well colocalized with mCherry-Theta toxin fragment, whatever the labeling sequence (Fig. S5C, D). In contrast, in normal and pre-malignant cells, domains were less abundant in control conditions but increased after chol depletion (Fig. 2A, B). Combination of data in the three cell lines with cell invasion potential shown in Fig. 1 indicated that the higher the surface chol content, the higher the extent of invasion (Fig. 2C). The specificity of m β CD towards the PM was proved by AFM since a slight decrease of the PM stiffness was observed but the cytocortex stiffness was preserved (Fig. 2D, E). Moreover, the effect of m β CD on cell invasion was reversed by chol repletion (light blue columns, Fig. 2F–H), as an additional argument against m β CD toxicity. In conclusion, the specific role of chol in malignant cell invasion could result from its increased content at the dorsal surface through the formation of submicrometric domains.

The dorsal surface cholesterol pool removed by methyl- β -cyclodextrin in malignant cells can be internalized by endocytosis and reach the ventral side

To then examine whether chol-enriched domains could also associate with the ventral surface of malignant cells near invadopodia, cells plated on glass or fibronectin-coated coverslips were compared for chol distribution at the dorsal side after labeling at 4, 20 and 37 °C. Fibronectin coating did not significantly affect the dorsal surface chol content as compared to glass coverslips, except for a slight decrease at 20 °C (Fig. S6 and filled columns vs striped columns in Fig. 2I). In contrast, increasing the temperature significantly decreased the dorsal chol content at the benefit of intracellular and ventral labeling (Fig. 2I and red vs yellow arrowheads in Fig. S6), suggesting endocytosis of the Theta toxin at 20 and 37 °C. This was confirmed by the observation that the majority of Theta-positive structures colocalized with LysoTracker

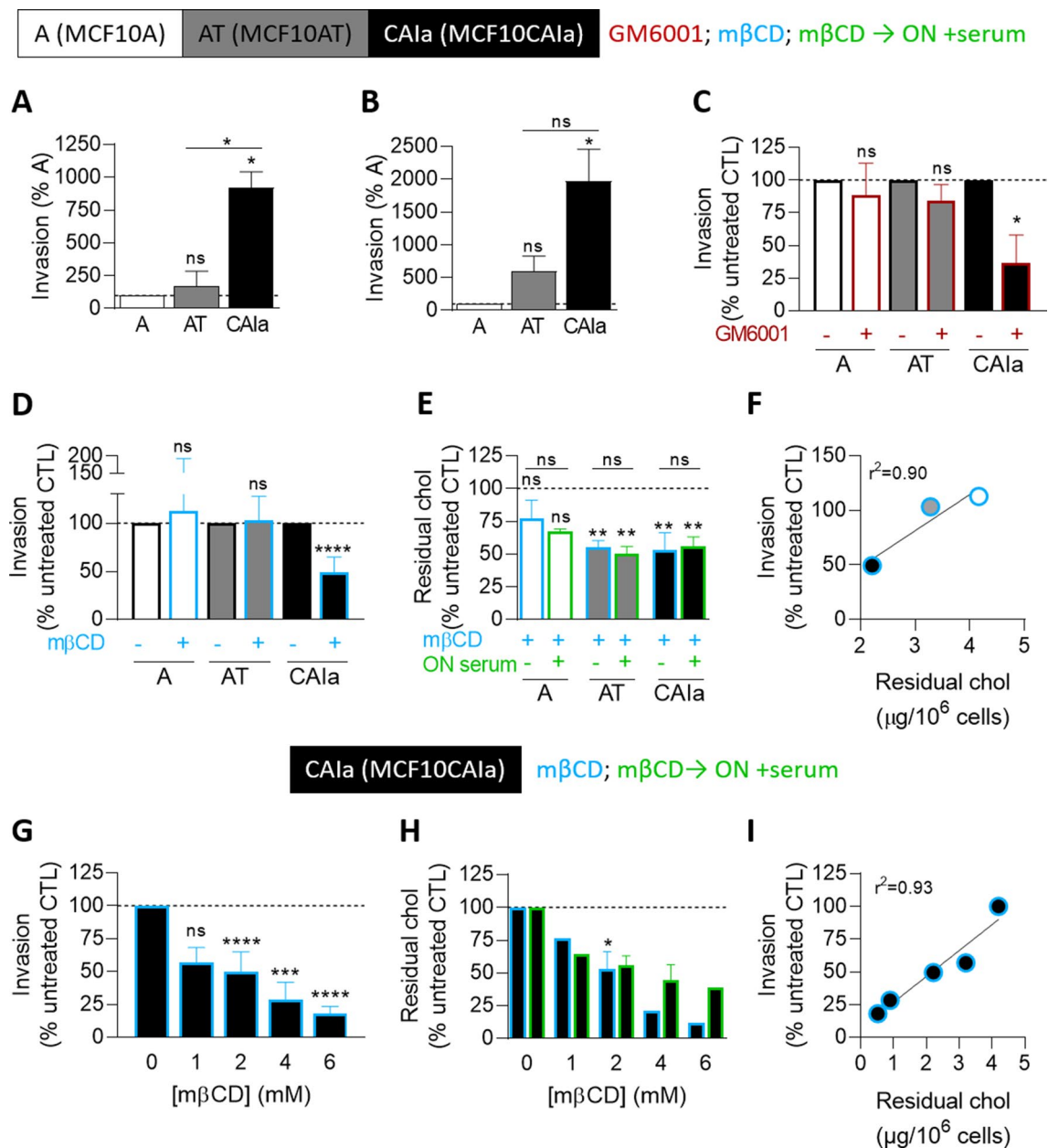


Fig. 1 The invasion of the malignant CAIa cells specifically depends on MMP activity and cholesterol content. **A–C** Quantification of invasion of the 3 cell lines in Transwell with a dense Matrigel layer toward 10% serum for 6–12 h (**A** $n=5-6$ Transwell from 4 independent experiments), 24 h (**B** $n=3-4$ Transwell from 3 independent experiments) or 6–12 h upon 10 μ M GM6001 to impair extracellular matrix degradation (**C** $n=4-7$ Transwell from 2 to 3 independent experiments). Kruskal–Wallis test followed by Dunn’s comparison test (**A**, **B**) or Mann–Whitney test (**C**). **D–I** Cell lines were treated with 2 mM (**D–F**) or the indicated concentrations of methyl- β -cyclodextrin (m β CD) for 2 h and then tested for invasion (**D**, **G**)

and residual chol content (**E**, **H**). Quantification of invasion of the 3 cell lines (**D**) or CAIa (**G**) in Transwell with a dense Matrigel layer toward 10% serum for 6–12 h ($n=4-19$ Transwell from 2 to 9 independent experiments). Unpaired t test (**D**) and Kruskal–Wallis test followed by Dunn’s comparison test (**G**). Residual chol content of the 3 cell lines (**E**) or CAIa (**H**) assessed by Amplex Red directly (blue border columns) or 12 h after m β CD treatment (ON, overnight; green border columns; $n=1-5$ independent experiments). Kruskal–Wallis test followed by Dunn’s comparison test (**E**, **H**). Linear correlation between the invasion of the 3 cell lines and their residual chol content (**F**); or between the invasion of CAIa and their residual chol (**I**)

in living CAIa cells colabeled with the Theta toxin and the LysoTracker to evidence acidic endocytic compartments (Fig. 2J idem and S7A). Moreover, inhibition of endocytosis by the dynamin inhibitor Dyngo4a reversibly

abrogated the redistribution of Theta clusters at the ventral side of CAIa cells (Fig. S7B, C). In addition, the m β CD-induced decrease of chol exposure previously observed at 4 $^{\circ}$ C was abrogated at 20 or 37 $^{\circ}$ C (Fig. S6

and blue border columns in Fig. 2I), suggesting that the chol pool that can be extracted by m β CD can reach the ventral face. This was confirmed by co-labeling CAIa cells with the Theta toxin and the SiR-actin probe. X–Z reconstructions showed the presence of chol at the ventral face in proximity with actin structures in untreated cells contrasting with its absence in m β CD-treated cells (Fig. 2K). Those observations suggested that the surface chol pool removed by m β CD can be internalized and reach the cell ventral face.

Partial membrane cholesterol removal in malignant cells does not impair the distribution of microtubules, intermediate filaments and focal adhesions but decreases invadopodia size and abundance

As malignant CAIa cells exhibit the lowest cytocortex stiffness and the highest chol surface content and invasion potential (Figs. 1B, 2B, S2A, D), we compared the cytoskeleton organization of the three cell lines and their interplay with chol. Immunolabeling of α -tubulin showed a similar spread pattern in the three cell lines that was not modified by chol depletion (Fig. S8A, S9A). Intermediate filament organization was differential in the three cell lines, with vimentin clustering around the nuclei in pre-malignant and malignant cells vs higher spreading in A cells, but also not affected by chol depletion (Fig. S9B). This differential pattern was accompanied by a distinct extent of vimentin dimerization (Fig. S8B, C). Focal adhesions revealed by paxillin immunolabeling were also differentially organized, with a lower number in malignant cells as compared to normal ones. Moreover, chol depletion strongly impaired the formation of focal adhesions in the normal cells but not in the malignant ones (Figs. 3A–D, S8D, S10A). Finally, invadopodia, which were revealed in CAIa cells by serum starvation followed by stimulation with serum-containing medium and immunolabeling for cortactin (Figs. S8E, S10B; [36]), were decreased in abundance and size upon chol depletion (Fig. 3E–H). In conclusion, chol depletion in malignant CAIa cells did not impair the distribution of microtubules, intermediate filaments and focal adhesions but decreased invadopodia size and abundance, suggesting that membrane chol could be involved in the formation of right-sized invadopodia.

Partial membrane cholesterol removal in malignant cells reversibly decreases extracellular matrix degradation

We next examined the consequences of m β CD-induced impaired invadopodia on ECM degradation using a gelatin degradation assay in cells plated on Oregon Green-coated coverslips, using the protocol of serum starvation and

immunolabeling described above. Malignant CAIa cells exhibited the highest gelatin degradation potential (Fig. 4A, B). Chol depletion in CAIa cells significantly decreased gelatin degradation in a reversible manner and similarly to MMP inhibition by GM6001 (Fig. 4C). Combination of m β CD and GM6001 treatments did not induce a stronger effect and the level of gelatin degradation potential of the three cell lines, untreated or not, positively correlated with the invasion potential (Fig. 4D). All those data suggested that m β CD and GM6001 could have the same target, potentially invadopodia sites.

The effects of cholesterol depletion on cell invasion, cholesterol surface exposure and invadopodia size in malignant CAIa cells are abrogated upon actin polymerization inhibition

As chol could be found in the proximity of ventral actin structures (Fig. 2K) and since chol controlled invadopodia size (Fig. 3E–H), we then tested if the actin cytoskeleton could in return control dorsal chol distribution. To test this hypothesis, cells were pretreated with m β CD, cytochalasin D (cytoD, an inhibitor of actin polymerization) or the combination of both drugs and assessed for invasion and for chol, focal adhesion and invadopodia distribution. CytoD disturbed F-actin organization particularly on the ventral side of malignant CAIa cells, decreased the size and abundance of focal adhesions in A and CAIa cells but did not significantly impact invadopodia in CAIa cells (pink at Fig. S11). Upon cytoD, invasion of the three cell lines was reduced but more strongly in CAIa cells and the surface chol content was only significantly decreased in CAIa cells (Fig. 5A, B). The latter effect could result from the intracellular chol sequestration evidenced by Theta labeling at 37 °C (pink in Fig. 5D), in agreement with [37]. Upon cytoD combined with m β CD, cell invasion and chol surface distribution were also affected in the same way (mauve at Fig. 5A, B), as confirmed by the strong and positive correlation between those two parameters (Fig. 5C). More importantly, inhibition of actin polymerization in the malignant cells decreased or even abrogated the m β CD-induced impaired invasion, chol surface exposure and invadopodia abundance and size (Fig. 5E–I, S12), suggesting an interplay between F-actin and chol functionality in the malignant cells.

The ER spreading and ER-organelle contact sites are more extended in malignant cells and perturbed by cholesterol depletion

As the mechanism behind the higher distribution of chol at the surface of CAIa cells, we hypothesized a differential organization of endoplasmic reticulum (ER)-PM contact sites which are involved in the regulation of lipid transport

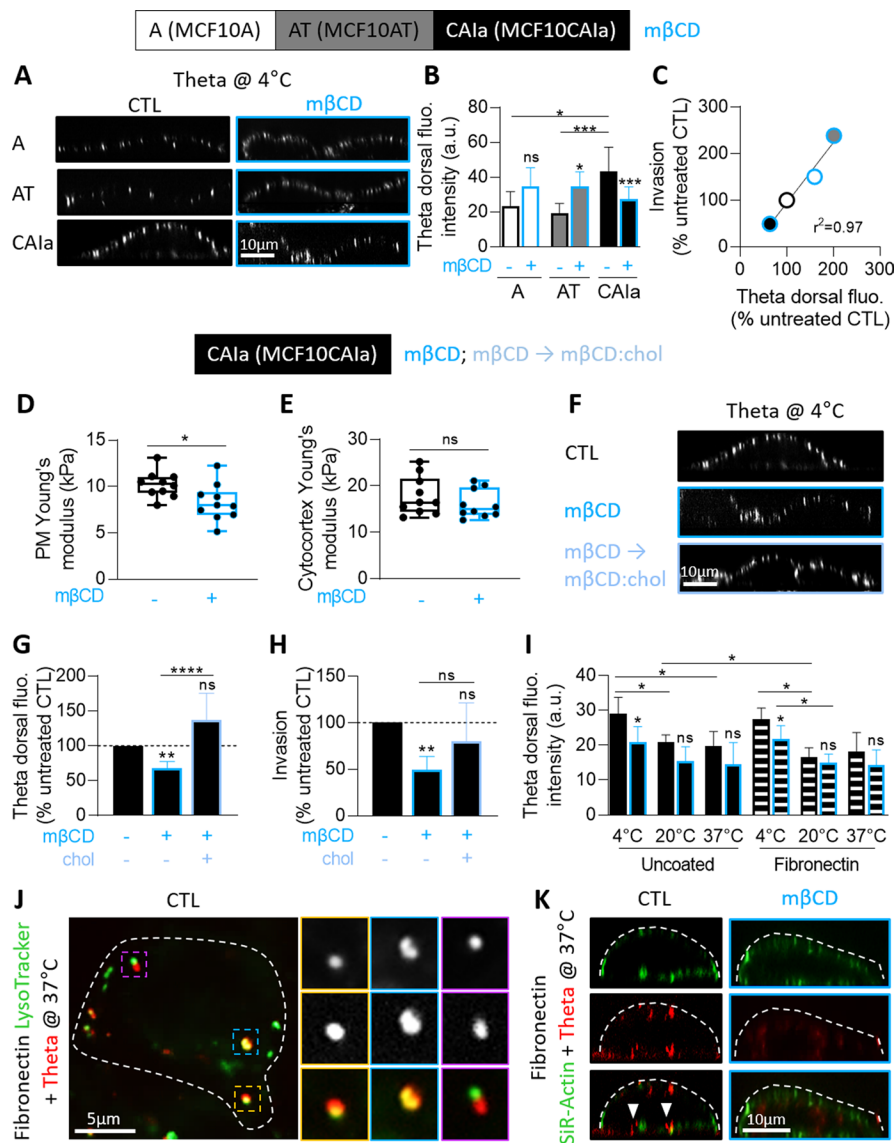


Fig. 2 In malignant CA1a cells, the dorsal cholesterol distributes in submicrometric domains that are specifically and reversibly decreased by methyl- β -cyclodextrin and can be endocytosed and reach the ventral face. Cell lines were treated or not (CTL, black) with 2 mM m β CD for 2 h (blue) or replenished with chol after depletion (light blue) and then tested for surface chol content (A–C, F, G, I, K), cell stiffness (D, E), cell invasion (H) and intracellular trafficking (J). (A, F) X–Z reconstructions of confocal images of the 3 cell lines (A) or CA1a (F) plated on glass coverslips, treated or not with m β CD followed or not by chol replenishment and labeled at 4 °C with the mCherry–Theta toxin fragment specific to endogenous chol. (B, G) Quantification of the Theta dorsal fluorescence intensity of the 3 cell lines or CA1a treated or not with m β CD followed by chol replenishment (average value of 10–15 cells from $n=2$ –28 images from 2 to 8 independent experiments and 15–20 cells from $n=8$ –14 images from 2 independent experiments). Mann–Whitney test (B) and Kruskal–Wallis test followed by Dunn’s comparison test (B, G). C Linear correlation between m β CD-treated invasion and Theta dorsal fluorescence intensity. (D, E) CA1a PM and cytocortex Young’s modulus determined by atomic force microscopy. Data points correspond to the mean values measured on a single cell (10 different cells) during $n \geq 3$ independ-

ent experiments. Mann–Whitney test. H Quantification of invasion of CA1a in Transwell with a dense Matrigel layer toward 10% serum for 12 h ($n=8$ –9 Transwell from 3 independent experiments). Kruskal–Wallis test followed by Dunn’s comparison test. I Quantification of the Theta dorsal fluorescence intensity of CA1a plated on glass (filled bars) or fibronectin-coated coverslips (striped bars), treated or not (black border columns) with m β CD (blue border columns) and labeled at 4, 20 or 37 °C with the mCherry–Theta toxin fragment (10–20 cells from $n=3$ –6 images from 1 experiment). Kruskal–Wallis test followed by Dunn’s comparison test and Mann–Whitney test. J Theta intracellular behavior determined by vital imaging at 37 °C on fibronectin-plated CA1a colabeled with the mCherry–Theta toxin fragment and the LysoTracker probe to label late endosomes/lysosomes. The first two insets show LysoTracker-positive compartments containing Theta-labeled chol whereas the third one shows a LysoTracker-negative Theta structure ($n=2$). K X–Z reconstructions of confocal images of CA1a plated on fibronectin-coated coverslips, treated or not with m β CD and colabeled at 37 °C with the mCherry–Theta toxin fragment and the SiR–Actin. Arrowheads, ventral chol-enriched domains ($n=1$)

a.o.. The three cell lines were thus immunolabeled for the ER marker KDEL and α -tubulin or cortactin to, respectively, reveal the whole cell or the ventral side (Fig. 6A, S13A). Whereas the ER was spread throughout the cytoplasm in malignant CAIa cells, it was more restricted to the perinuclear region in A and AT cells. Upon m β CD, the opposite situation was seen with a higher spreading in A and AT cells as compared to the CAIa cells (Fig. 6A, D).

To then explore whether the differential ER spreading in the three cell lines could be accompanied by differential ER-mitochondria contact sites, we analyzed the distribution of the ER vs Ca^{2+} ions in living cells using an ER-Tracker and Fluo4-AM. Mitochondria are indeed associated with Ca^{2+} handling [38]. The Fluo4-positive structures exhibited a tubular structure typical of mitochondria in normal cells but a more rounded morphology in pre-malignant and malignant cells, in agreement with [39]. Moreover, the contact/localization between those Ca^{2+} -enriched structures and the ER was more visible in malignant cells than in normal and pre-malignant ones and was decreased by chol depletion (Fig. 6B). We finally explored the ER-endocytic compartment contact sites by KDEL immunolabeling in Lysotracker-labeled cells. The Lysotracker-positive structures were less abundant (Fig. S13B) and exhibited a wider and more aligned distribution and closer contacts with the ER in malignant cells than A and AT cells. All those particularities were abrogated by m β CD (Figs. 6C, E, S13C). Altogether, those data suggested that the extent of ER-PM and ER-organelle contact sites were differentially regulated in malignant cells and were dependent on the chol content.

MDA-MB-231 cells also depend on cholesterol for invasion, invadopodia size and gelatin degradation

To finally explore the relevance of our data for a more common mutation in breast cancer, analyses were extended to the highly invasive triple-negative MDA-MB-231 cell line. Like malignant CAIa cells, MDA-MB-231 cells exhibited a high invasion potential that depended on both MMP activity and chol content (Fig. 7A, B). Theta labeling on both glass and fibronectin-coated coverslips revealed a similar dorsal chol distribution to CAIa cells. Moreover, this dorsal chol was decreased by temperature increase and chol depletion at 4 °C but not at 37 °C (Fig. 7C). Although the abundance of invadopodia was not impacted by chol depletion, their size was decreased (Fig. 7D, F–H). The ECM degradation was also decreased in a reversible manner and a combination of m β CD and GM6001 treatments did not induce a stronger effect than GM6001 alone, as in CAIa cells (Fig. 7E, I). Altogether, the importance of membrane chol for malignant cell invasion through matrix degradation

and right-sized invadopodia formation was confirmed in another invasive breast cancer cell line, the MDA-MB-231 cells.

Discussion

Main observations

Using the MCF10A cell line series as a model of breast cancer progression, we have previously reported higher PM stiffness and surface chol content of malignant CAIa cells compared to normal A and pre-malignant AT cells [23]. We here showed that the malignant CAIa cells specifically exhibited submicrometric chol-enriched domains at their surface and chol-dependent narrow contact sites between the ER and PM organelles. This specific organization was required for the control of cell invasion. Mechanistically, chol-enriched submicrometric domains reached the cell ventral face where they were involved in invadopodia maturation and ECM degradation. Chol surface distribution and chol-dependent control of invadopodia and invasion were similarly observed in MDA-MB-231 cells but contrasted with the lower surface chol exposure and the chol-dependent control of focal adhesions in non-malignant cells.

Cholesterol forms two types of submicrometric domains at the surface of malignant cell lines

Conflicting data regarding the deregulation of chol in cancer arise in the literature. On one hand, cancer cells exhibit a reprogrammed chol metabolism notably due to enhanced chol biosynthesis [17, 40]. On the other hand, lower chol levels in the human liver and breast cancer cell lines lead to increased membrane fluidity and promote migration and invasion [41–43]. By directly comparing cell lines with the same genetic background, we showed that despite a similar chol content in malignant vs non-malignant cells, malignant cells exhibited a ~50% increase of chol at the external PM leaflet and its clustering in submicrometric domains.

Due to the high threshold required for chol Theta toxin binding (~30 mol%), domains should present a very high chol content [20]. Domain abundance is decreased by ~35% with 2 mM m β CD, in the same order of magnitude than the ~45% reduction of the total chol content. Based on those data, our previous data on living red blood cells and myoblasts [20] and the work of Das and coll. on fibroblasts [44], we suggested that two types of chol-enriched domains coexist at the malignant cell surface. The first one is sensitive to m β CD and corresponds to the labile pool described by Das et al., while the second one cannot be removed by m β CD and represents the non-labile pool. This former pool can be internalized, as revealed by

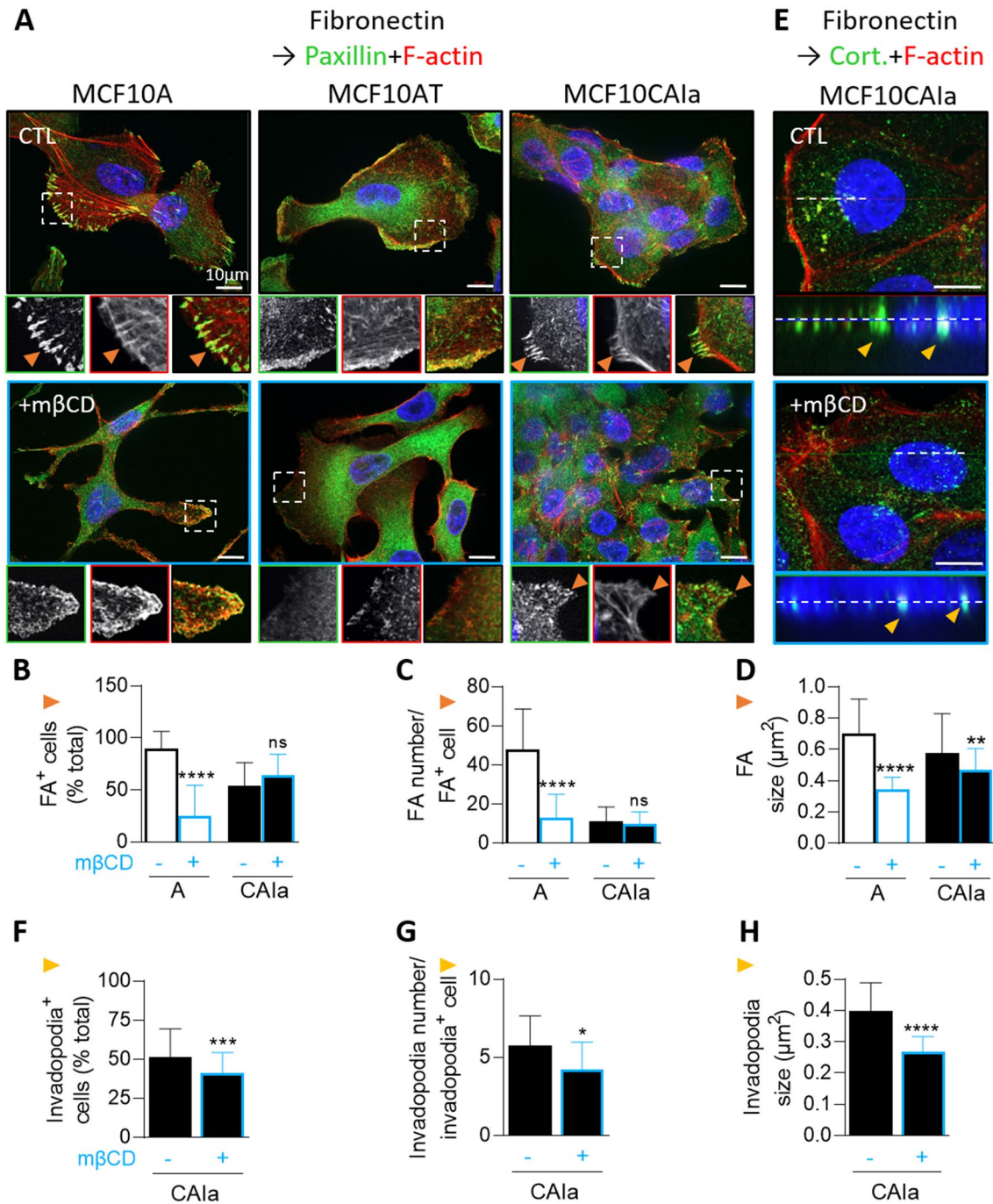


Fig. 3 Cholesterol depletion in malignant CA1a cells does not affect focal adhesions but reduces invadopodia size and abundance. Cell lines were plated on fibronectin-coated coverslips, treated with 2 mM mβCD for 2 h (blue), immunolabeled for paxillin (**A–D**) or cortactin (**E–H**), analyzed by confocal microscopy and quantified. **A–E** Confocal images of the 3 cell lines (**A**) or CA1a (**E**) immunolabeled with anti-Paxillin or anti-Cortactin together with F-actin (stained by Phalloidin) and nuclei (stained with Hoechst). Insets in **A** and orange arrowheads show paxillin-positive focal adhesions (FA). Insets in **E**

and yellow arrowheads show X–Z reconstructions of invadopodia length along the dotted line. **B–D** Quantifications of the number of A and CA1a cells presenting focal adhesions, the number of focal adhesions per cell and the focal adhesion size [$n=27–35$ images (**B**) and $n=44–84$ cells (**C**, **D**) from 4–5 independent experiments]. **F–H** Quantifications of the number of CA1a cells presenting invadopodia, the number of invadopodia per cell and the invadopodia size ($n=16–65$ images from 2 independent experiments). Unpaired t test

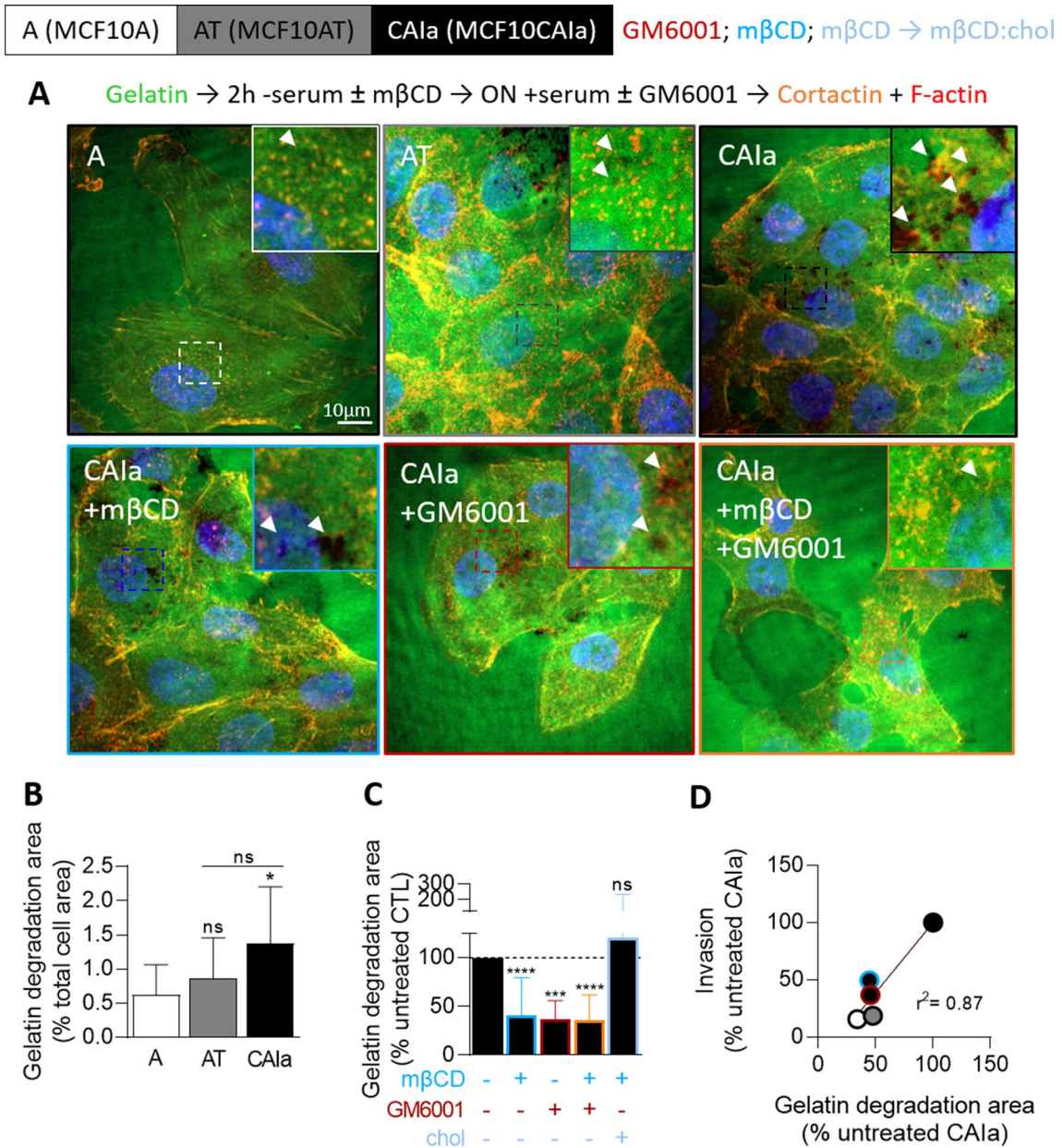


Fig. 4 Cholesterol depletion in malignant CAIa cells reduces gelatin degradation to a similar extent than MMP inhibition. Cell lines were plated on Oregon Green-coated coverslips, serum-starved combined or not with 2 mM mβCD (blue) for 2 h, then repleted or not with chol for 1 h (light blue). Cells were then stimulated overnight (ON) with serum-containing medium supplemented or not with GM6001 (red) and then tested for gelatin degradation. **A** Representative images of gelatin degradation (black areas; arrowheads) of cells (immuno) labeled with anti-Cortactin, F-actin (Phalloidin) and nuclei (Hoechst).

B, C Quantification of gelatin degradation potential of the 3 cell lines (**B** 5–20 cells from $n=8-12$ images from 1 experiment) or CAIa treated or not with mβCD, GM6001 or the combination of both drugs or repleted with chol (**C** 10–30 cells from $n=9-50$ images from 1 to 4 independent experiments). Kruskal–Wallis test followed by Dunn’s comparison test. **D** Linear correlation between the invasion of the 3 cell lines and CAIa treated with mβCD in combination or not with GM6001 and gelatin degradation potential

the abrogation of mβCD effect on chol-enriched domain redistribution from the dorsal to the ventral face upon temperature increase. Moreover, the chol content of those domains appeared to depend on the actin cytoskeleton, since actin polymerization inhibition by cytoD removed ~35% of the PM chol specifically in malignant cells

and without potentiating the effect of mβCD. The interplay between chol and the actin cytoskeleton has been recently suggested. For instance, disruption of the actin cytoskeleton leads to the movement of sterols from the PM to endosomes [37]. Moreover, the knockout of ORP2, an oxysterol binding protein (OSBP)-related protein

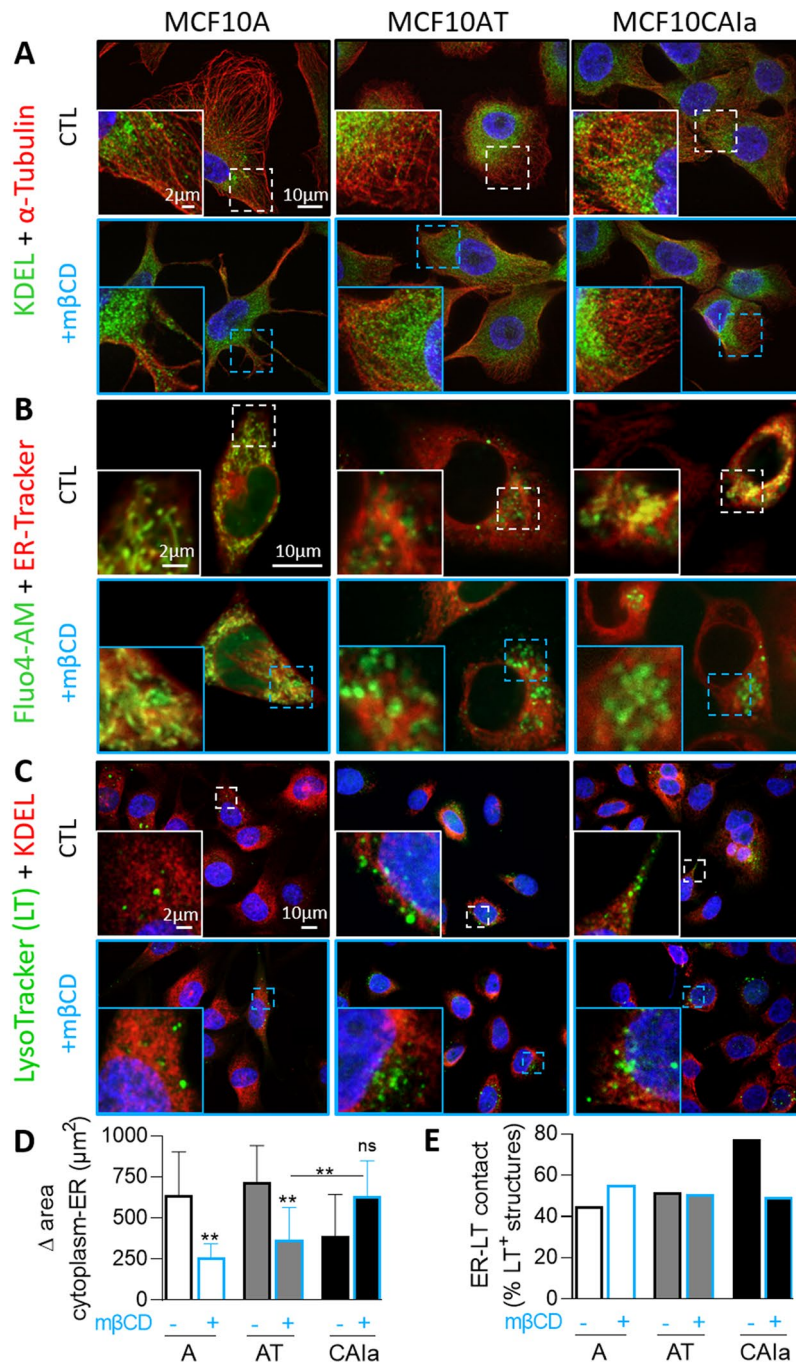


Fig. 6 The higher endoplasmic reticulum network spreading and its closer contact with mitochondria/lysosomes in malignant cells than in normal and premalignant cells are lost upon cholesterol depletion. The 3 cell lines were plated on fibronectin-coated coverslips, treated or not with 2 mM m β CD for 2 h (blue) and analyzed by confocal microscopy. **A** Coimmunolabeling with anti-KDEL (endoplasmic reticulum; ER) and anti- α -Tubulin (microtubules, to reveal the whole cytoplasm). Nuclei stained with Hoechst. **B** Colabeling at 37 °C with the Fluo4-AM specific to Ca²⁺ and the ER-Tracker. **C** labeling at 37°C with the LysoTracker (LT) specific to late endosomes/lysosomes followed by immunolabeling with anti-KDEL. **D** Quantification of the ER network spreading of the 3 cell lines treated or not (black border columns) with 2 mM m β CD for 2 h (blue border columns). Data are expressed as the difference of area between the whole cytoplasm and the ER ($n=12-47$ cells from $n=7-8$ images from 1 experiment). Kruskal–Wallis test followed by Dunn’s comparison test and Mann–Whitney test. **E** Quantification of the number of LysoTracker (LT) positive structures in close contact with the ER in the 3 cell lines treated or not (black border columns) with 2 mM m β CD for 2 h (blue border columns). Data are expressed as ER-LysoTracker (LT) contact structures reported to total LysoTracker positive structures ($n=29-50$ profiles from 8 to 14 images from 1 experiment)

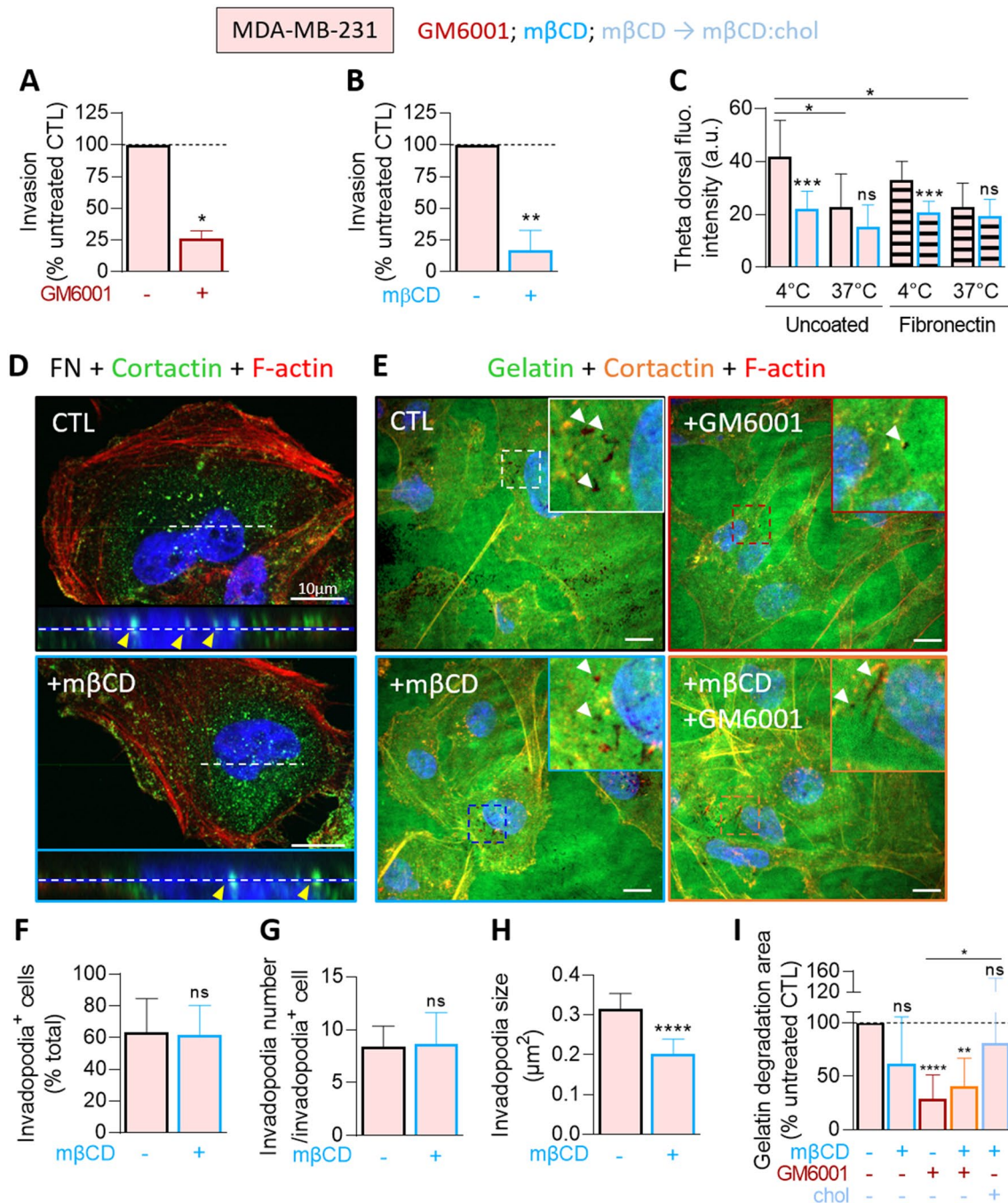


Fig. 7 Malignant MDA-MB-231 cells also present high surface cholesterol distribution and depend on cholesterol for invasion, invadopodia size and gelatin degradation. MDA-MB-231 were treated with 2 mM of mβCD (blue) in combination or not with 10 μM GM6001 (red) or repleted with chol for 1 h (light blue) and then tested for invasion (**A**, **B**), surface chol content (**C**), invadopodia formation (**D**, **F–H**) and gelatin degradation (**E**, **I**). **A**, **B** Quantification of invasion in Transwell with a dense Matrigel layer toward 10% serum for 12 h upon GM6001 or after 2 h of mβCD ($n=4–5$ Transwell from 2 independent experiments and $n=6$ from 3 independent experiments, respectively). Mann–Whitney test. **C** Quantification of Theta dorsal fluorescence intensity of MDA-MB-231 plated on glass (filled bars) or fibronectin-coated coverslips (striped bars), treated or not (black border columns) with mβCD (blue border columns) and labeled at

4 or 37 °C with the mCherry-Theta toxin fragment (7–15 cells from $n=8–11$ images from 2 independent experiments). Mann–Whitney test. **D**, **E** Confocal images of MDA-MB-231 plated on fibronectin (FN)-coated or Oregon Green-coated coverslips, treated as described in Figs. 3E and 4 and immunolabeled with anti-Cortactin together with F-Actin (Phalloidin) and nuclei (Hoechst). Insets in **D** show X–Z reconstructions of invadopodia length along the dotted line. **F–H** Quantification of the number of cells presenting invadopodia, the number of invadopodia per cell and the invadopodia size from images presented in **D** ($n=12–35$ images from 2 independent experiments). Unpaired *t* test. **I** Quantification of gelatin degradation potential from images presented in **E** (8–15 cells from $n=10–46$ images from 1 to 4 independent experiments). One-Way ANOVA test followed by Dunnett’s comparison test

identified as a unique transporter of the labile chol pool from the ER to the PM [45], impairs hepatoma cell migration and adhesion through disorganization of F-actin and lamellipodia [46].

Cholesterol surface exposure in malignant cells associates with narrow membrane contact sites

Converging evidences in the literature indicate that, after synthesis in the ER, the transport of chol is fast and carried between membranes by lipid transfer proteins. We here showed that the ER-PM contact sites were more extended in the malignant cells, in agreement with their proposed role in cancer progression [47, 48]. Moreover, chol depletion decreased both ER-PM contacts and chol surface exposure, consistent with the accumulation of ER-resident proteins at ER-PM contact sites upon chol supplementation [49, 50].

Those data led us to suggest that the increased surface chol content in malignant cells could result from an increase in chol biosynthesis in the ER, followed by exchanges at the ER-PM contact sites. Nevertheless, the total chol content was not increased in malignant cells and ER-anchored lipid transfer proteins should sense and transport accessible PM chol to the ER to maintain lipid homeostasis. Therefore, the mechanism behind the higher cell surface chol exposure should be far from more complex, involving chol PM retention through two non-mutually exclusive potential scenarios.

The first scenario implies chol PM-to-endosome retrograde trafficking and its return to the PM by a vesicular trafficking-independent mechanism. This sterol flow, which has been recently identified in yeast, involves the ER [37]. Accordingly, ER-endosome contact sites are implied in chol exchange through ORP1L, another member of the OSBP family [51]. Three pieces of data specifically observed in malignant cells supported this hypothesis, *i.e.* the extended ER spreading, the chol-dependent ER-PM and ER-endosomes contacts and the partial redistribution of chol from the cell surface to intracellular structures upon actin polymerization impairment.

The second scenario proposes that, after the exchange at ER-PM contact sites, chol is rapidly transferred to the outer PM leaflet, preserving it from retrograde transport from the PM inner leaflet to the ER. Although the transversal PM distribution of chol is far from well understood, sterols have been proposed to partition in the outer leaflet according to their affinity for sphingolipids or in the inner leaflet driven by positive interactions with PE or PS [52]. The fact that PE is less abundant in invasive MCF10CA1a cells compared to premalignant cells [15] and that the cytocortex stiffness is lower in malignant cells compared to pre-malignant and normal ones [23] supported the possibility of a lower chol retention in the inner PM.

Cholesterol surface exposure in malignant cells specifically controls invasion

The invasion potential of the two invasive cell lines, the CA1a and MDA-MB-231, was specifically and reversibly inhibited by chol depletion. The contribution of chol in cell migration/invasion is not new but data are often contradictory. Indeed, chol depletion has been shown to reduce breast cancer cell lines migration [53, 54] while its supplementation promotes migration and invasion of renal carcinoma cells [55]. Conversely, lower membrane chol content correlates with increased invading capacity compared to non-invading cells [13, 19].

In addition, the specificity towards malignant *vs* non-malignant cells and the mechanisms behind the implication of chol are far from well understood. We here proved the specific role of chol in the invasion of malignant cells through the comparison with normal and pre-malignant ones. Mechanistically, we evidenced that chol-enriched surface domains played a key role in breast cancer cell invasion, as supported by the following lines of evidence. First, through the use of m β CD combined with imaging with validated chol probes, we showed that the high chol surface and invasion extent were similarly impaired by chol depletion, specifically in malignant cells. Second, the effect of m β CD on cell invasion was abrogated in cytoD-treated malignant cells and accompanied by a reduced chol surface exposure. Thus, we revealed the implication of chol surface content in cell invasion, a conclusion supported by the excellent correlation between those two parameters, whatever the cell line and the pharmacological treatment (Fig. 8A).

Cholesterol surface exposure in malignant cells controls invadopodia maturation and ECM degradation

Previous studies have shown that PM chol appropriate levels in human melanoma cells and caveolin-1 in breast cancer cells regulate the formation and function of invadopodia [56, 57] and that disruption of lipid rafts by m β CD suppresses invadopodia formation and breast cancer cell invasion [58]. Nevertheless, those conclusions were mostly based on indirect evidences. Combining the Theta toxin fragment at different temperatures to label both the surface and intracellular chol pools with chol modulation approaches, we here showed that the high chol surface exposure in malignant cells contributed to control invasion through right-sized invadopodia and ECM degradation. Invadopodia formation requires three phases. The initiation phase is characterized by the assembly of actin-based precursor complexes and cortactin-dependent actin polymerization that extends the PM and drives elongation of cellular protrusions and is facilitated by microtubules and intermediate filaments. During the stabilization phase,

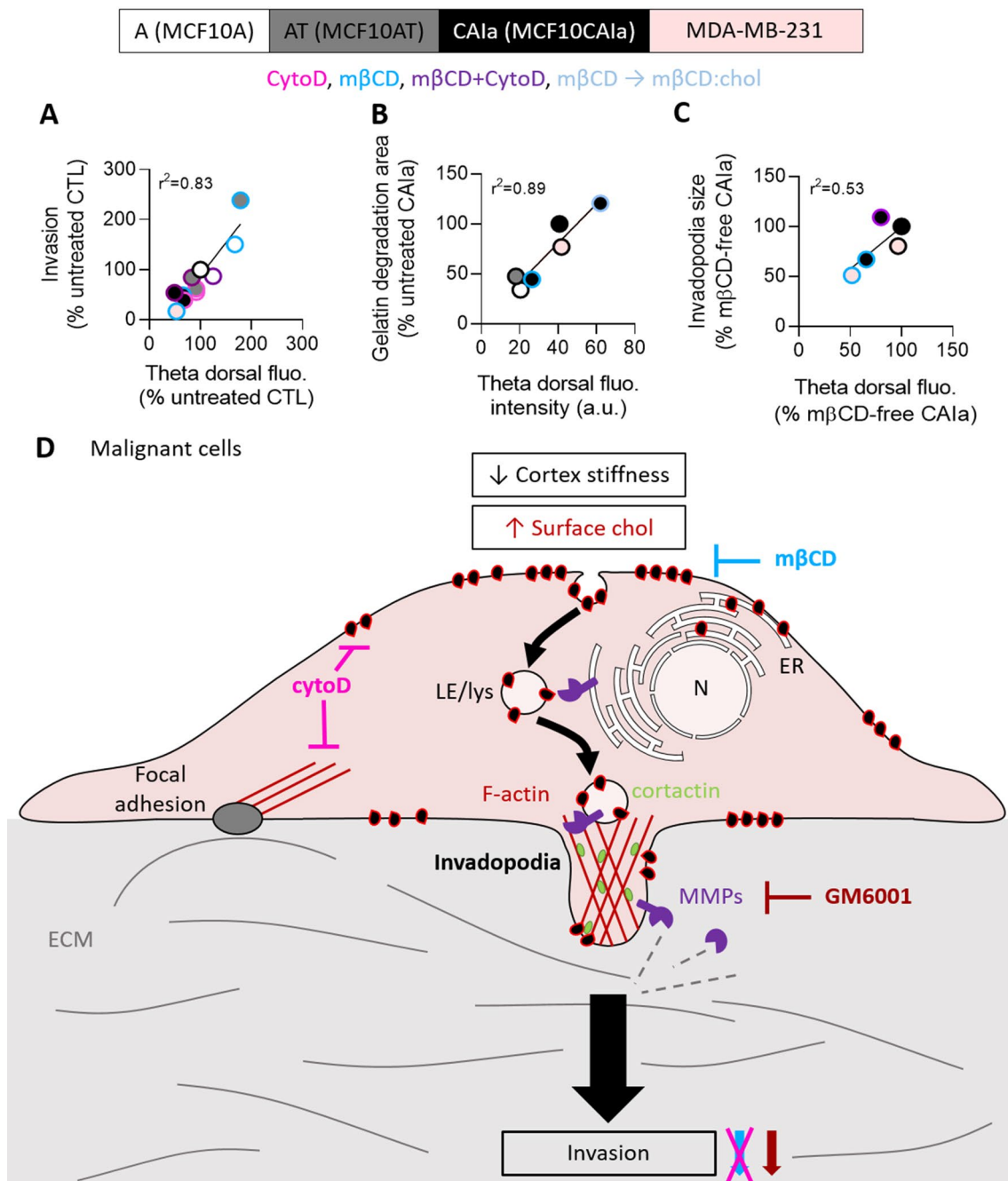


Fig. 8 Hypothetical model. Positive linear correlations between the Theta dorsal fluorescence intensity and cell invasion (A), gelatin degradation potential (B) and invadopodia size (C) in MCF10A (white), AT (grey), CAIa (black) and MDA-MB-231 (light pink) treated with mβCD (blue border) in combination (purple border) or not with cytoD (pink border) or replenished with chol (light blue border). **D** Hypothetical model for the implication of membrane chol-enriched domains in malignant cell invasion through their endocytosis from

the dorsal side, exchange of MMPs at ER-late endosome/lysosome contact sites and transport into invadopodia. In addition, dorsal and ventral chol-enriched domains could also contribute to invadopodia signaling events (not shown). For additional information, see discussion. N, nucleus; ECM, extracellular matrix; ER, endoplasmic reticulum; LE, late endosome; Lys, lysosome. Thick arrows, pathway favored in malignant vs non-malignant cells

actin filaments are crosslinked into tightly packed bundles and anchored to PM to form a stable 3D functional structure. During the maturation phase, MMPs are recruited to invadopodia, allowing for local ECM degradation. Our data

indicated that chol depletion did affect neither microtubules, intermediate filaments and invadopodia abundance nor ECM degradation area formation but decreased the size of both invadopodia and ECM degradation area in correlation with

the residual chol content (Fig. 8B, C). This suggested no effect on the initiation phase but impairment of invadopodia maturation, a step known to depend on anterograde transport of MT1-MMP [36]. This proteolytic enzyme is, like PM chol, endocytosed by clathrin- and caveolin-dependent pathway [59], depends on the aggregation of F-actin and cortactin to accumulate at invadopodia [60], associates with lipid rafts [57] and depends on membrane contacts with the ER-resident protein protrudin to mediate ECM degradation [36]. In support of the above hypothesis, we found that dorsal chol-enriched domains can reach the malignant cell ventral side by endocytosis and that contact sites between the ER and late endosomes/lysosomes in malignant cells were closer and chol-dependent. We thus suggested that chol-enriched domains contribute to malignant cell invasion through their endocytosis from the cell dorsal side, exchange of MMPs at ER-late endosome/lysosome contact sites and transport at the ventral side into invadopodia (Fig. 8D).

As a non-mutually exclusive mechanism, chol-enriched domains could contribute to signaling events at the different stages of invadopodia formation and maturation which are under distinct but interconnected signaling control mechanisms. For instance, growth factor signaling promotes the formation of invadopodia, whereas adhesion to the ECM promotes localized protease exocytosis [61]. Several studies support the role of chol-enriched domains in growth factor receptor distribution, endocytosis and signaling at the PM. Thus, using single-molecule optical tracking, Lin and coll. have revealed chol-mediated interactions between activated EGFRs at the surface of living cells [62]. In prostate tumor cells, the EGFR is phosphorylated and more active within membrane rafts [63]. In live CHO-K1 PM, part of EGFR in the resting state is trapped in chol-containing domains and after disruption of those domains, EGF induces microscopic EGFR clusters and endocytosis is inhibited [64]. In ovarian carcinoma cells in 3D collagen, EGFR and MT1-MMP colocalize with caveolae prior to activation and stimulation with EGF disrupts their association and leads to MT1-MMP internalization [65]. In addition, MT1-MMP associates with lipid rafts [57], can activate the pro-MMP-2 through the formation of a complex with the pro-MMP2 and the tissue inhibitor of metalloproteinases-2 TIMP-2 and can process cell adhesion molecules [66].

Cholesterol in non-invasive cells controls focal adhesions

The high surface chol, the chol- and MMP-dependent invasion and the narrow chol-dependent ER-organelle/PM contact sites in malignant cells contrasted with the lower surface chol exposure, the MMP- and chol-independent invasion and the looser membrane contact sites in non-invasive

cells. Moreover, in contrast to its effect in malignant cells, chol depletion increased both the ER spreading and the chol surface exposure in non-malignant cells. These findings agreed with the drastic increase of ER-PM association in yeast and the extension of the ER tubules and redistribution of lysosomes to the cell periphery upon sterol depletion [67, 68]. Another contrast between malignant and non-malignant cells was the chol-dependent control of invadopodia vs focal adhesions and low invasion. These findings were consistent with the observation that the LDL-chol is delivered to the PM in close proximity of focal adhesions by the Rab8a-MyosinVb-actin pathway, favoring focal adhesion abundance and dynamics and promoting cell migration [69].

Conclusion

Our data indicated the key contribution of chol-enriched surface domains in the control of invasion of breast cancer cell lines, providing new clues for the understanding of the molecular events underlying cellular mechanisms in breast cancer.

Supplementary Information The online version contains supplementary material available at <https://doi.org/10.1007/s00018-022-04426-8>.

Acknowledgements We thank Drs. A. Miyawaki, M. Abe and T. Kobayashi (Riken Brain Science Institute, Saitama, Japan and University of Strasbourg, France) as well as H. Mizuno (KU Leuven, Belgium) for generously supplying the Dronpa-Theta-D4 plasmid. We also thank Dr. NE. Sounni (Uliège) for providing us MDA-MB-231 cell line.

Author contributions MM, MPM, DA and DT designed the experiments. MM and DT analyzed and interpreted the data and wrote the manuscript. DM, ACD and DA generated and analyzed AFM data. ML and SV performed and quantified Western blotting and Chol assay. All authors reviewed the final version of the manuscript.

Funding This work was supported by grants from the UCLouvain (FSR and Actions de Recherches concertées, ARC), the F.R.S-FNRS and the Télévie.

Data availability All data are available and the manuscript includes supplemental information submitted electronically.

Declarations

Conflict of interest The authors declare no competing financial interests.

Open Access This article is licensed under a Creative Commons Attribution 4.0 International License, which permits use, sharing, adaptation, distribution and reproduction in any medium or format, as long as you give appropriate credit to the original author(s) and the source, provide a link to the Creative Commons licence, and indicate if changes were made. The images or other third party material in this article are included in the article's Creative Commons licence, unless indicated otherwise in a credit line to the material. If material is not included in the article's Creative Commons licence and your intended use is not

permitted by statutory regulation or exceeds the permitted use, you will need to obtain permission directly from the copyright holder. To view a copy of this licence, visit <http://creativecommons.org/licenses/by/4.0/>.

References

- Lekka M, Laidler P, Gil D, Lekki J, Stachura Z, Hryniewicz AZ (1999) Elasticity of normal and cancerous human bladder cells studied by scanning force microscopy. *Eur Biophys J* 28(4):312–316. <https://doi.org/10.1007/s002490050213> (Epub 1999/07/08. PubMed PMID: 10394623)
- Guck J, Schinkinger S, Lincoln B, Wottawah F, Ebert S, Romeyke M et al (2005) Optical deformability as an inherent cell marker for testing malignant transformation and metastatic competence. *Biophys J* 88(5):3689–3698. <https://doi.org/10.1529/biophysj.104.045476> (Epub 2005/02/22. PubMed PMID: 15722433; PubMed Central PMCID: PMCPMC1305515)
- Lekka M, Gil D, Pogoda K, Dulinska-Litewka J, Jach R, Gostek J et al (2012) Cancer cell detection in tissue sections using AFM. *Arch Biochem Biophys* 518(2):151–156. <https://doi.org/10.1016/j.abb.2011.12.013> (Epub 2012/01/03. PubMed PMID: 22209753)
- Lekka M (2016) Discrimination between normal and cancerous cells using AFM. *Bionanoscience* 6:65–80. <https://doi.org/10.1007/s12668-016-0191-3> (Epub 2016/03/26. PubMed PMID: 27014560; PubMed Central PMCID: PMCPMC4778153)
- Runel G, Lopez-Ramirez N, Chlasta J, Masse I (2021) Biomechanical properties of cancer cells. *Cells*. <https://doi.org/10.3390/cells10040887> (Epub 2021/05/01. PubMed PMID: 33924659; PubMed Central PMCID: PMCPMC8069788)
- Szlaza W, Zendran I, Zalesinska A, Tarek M, Kulbacka J (2020) Lipid composition of the cancer cell membrane. *J Bioenerg Biomembr* 52(5):321–342. <https://doi.org/10.1007/s10863-020-09846-4> (Epub 2020/07/28. PubMed PMID: 32715369; PubMed Central PMCID: PMCPMC7520422)
- Kundu M, Mahata B, Banerjee A, Chakraborty S, Debnath S, Ray SS et al (2016) Ganglioside GM2 mediates migration of tumor cells by interacting with integrin and modulating the downstream signaling pathway. *Biochim Biophys Acta* 1863(7 Pt A):1472–1489. <https://doi.org/10.1016/j.bbamcr.2016.04.004> (Epub 2016/04/14. PubMed PMID: 27066976)
- Perrotti F, Rosa C, Cicalini I, Sacchetta P, Del Boccio P, Genovesi D et al (2016) Advances in lipidomics for cancer biomarkers discovery. *Int J Mol Sci*. <https://doi.org/10.3390/ijms17121992> (Epub 2016/12/06. PubMed PMID: 27916803; PubMed Central PMCID: PMCPMC5187792)
- Bernardes N, Fialho AM (2018) Perturbing the dynamics and organization of cell membrane components: a new paradigm for cancer-targeted therapies. *Int J Mol Sci*. <https://doi.org/10.3390/ijms19123871> (Epub 2018/12/07. PubMed PMID: 30518103; PubMed Central PMCID: PMCPMC6321595)
- Canals D, Hannun YA (2013) Novel chemotherapeutic drugs in sphingolipid cancer research. *Handb Exp Pharmacol* 215:211–238. https://doi.org/10.1007/978-3-7091-1368-4_12 (Epub 2013/04/13. PubMed PMID: 23579458; PubMed Central PMCID: PMCPMC3998523)
- Rysman E, Brusselmans K, Scheys K, Timmermans L, Derua R, Munck S et al (2010) De novo lipogenesis protects cancer cells from free radicals and chemotherapeutics by promoting membrane lipid saturation. *Cancer Res* 70(20):8117–8126. <https://doi.org/10.1158/0008-5472.CAN-09-3871> (Epub 2010/09/30. PubMed PMID: 20876798)
- Connor J, Bucana C, Fidler IJ, Schroit AJ (1989) Differentiation-dependent expression of phosphatidylserine in mammalian plasma membranes: quantitative assessment of outer-leaflet lipid by prothrombinase complex formation. *Proc Natl Acad Sci USA* 86(9):3184–3188. <https://doi.org/10.1073/pnas.86.9.3184> (Epub 1989/05/01. PubMed PMID: 2717615; PubMed Central PMCID: PMCPMC287091)
- Zeisig R, Koklic T, Wiesner B, Fichtner I, Sentjurs M (2007) Increase in fluidity in the membrane of MT3 breast cancer cells correlates with enhanced cell adhesion in vitro and increased lung metastasis in NOD/SCID mice. *Arch Biochem Biophys* 459(1):98–106. <https://doi.org/10.1016/j.abb.2006.09.030> (Epub 2007/01/16. PubMed PMID: 17222386)
- Wang S, Chen X, Luan H, Gao D, Lin S, Cai Z et al (2016) Matrix-assisted laser desorption/ionization mass spectrometry imaging of cell cultures for the lipidomic analysis of potential lipid markers in human breast cancer invasion. *Rapid Commun Mass Spectrom* 30(4):533–542. <https://doi.org/10.1002/rcm.7466> (Epub 2016/01/19. PubMed PMID: 26777684)
- Vidavsky N, Kunitake J, Diaz-Rubio ME, Chiou AE, Loh HC, Zhang S et al (2019) Mapping and profiling lipid distribution in a 3D model of breast cancer progression. *ACS Cent Sci* 5(5):768–780. <https://doi.org/10.1021/acscentsci.8b00932> (Epub 2019/05/30. PubMed PMID: 31139713; PubMed Central PMCID: PMCPMC6535773)
- Hilvo M, Denkert C, Lehtinen L, Muller B, Brockmoller S, Seppanen-Laakso T et al (2011) Novel theranostic opportunities offered by characterization of altered membrane lipid metabolism in breast cancer progression. *Cancer Res* 71(9):3236–3245. <https://doi.org/10.1158/0008-5472.CAN-10-3894> (Epub 2011/03/19. PubMed PMID: 21415164)
- Ehmsen S, Pedersen MH, Wang G, Terp MG, Arslanagic A, Hood BL et al (2019) Increased cholesterol biosynthesis is a key characteristic of breast cancer stem cells influencing patient outcome. *Cell Rep* 27(13):3927–38 e6. <https://doi.org/10.1016/j.celrep.2019.05.104> (Epub 2019/06/27. PubMed PMID: 31242424)
- Peetla C, Vijayaraghavalu S, Labhassetwar V (2013) Biophysics of cell membrane lipids in cancer drug resistance: implications for drug transport and drug delivery with nanoparticles. *Adv Drug Deliv Rev* 65(13–14):1686–1698. <https://doi.org/10.1016/j.addr.2013.09.004> (Epub 2013/09/24. PubMed PMID: 24055719; PubMed Central PMCID: PMCPMC3840112)
- Sok M, Sentjurs M, Schara M, Stare J, Rott T (2002) Cell membrane fluidity and prognosis of lung cancer. *Ann Thorac Surg* 73(5):1567–1571. [https://doi.org/10.1016/s0003-4975\(02\)03458-6](https://doi.org/10.1016/s0003-4975(02)03458-6) (Epub 2002/05/23. PubMed PMID: 12022551)
- Carquin M, Conrard L, Pollet H, Van Der Smissen P, Cominelli A, Veiga-da-Cunha M et al (2015) Cholesterol segregates into submicrometric domains at the living erythrocyte membrane: evidence and regulation. *Cell Mol Life Sci* 72(23):4633–4651. <https://doi.org/10.1007/s00018-015-1951-x> (Epub 2015/06/17. PubMed PMID: 26077601)
- Pollet H, Cloos AS, Stommen A, Vanderroost J, Conrard L, Paquot A et al (2020) Aberrant membrane composition and biophysical properties impair erythrocyte morphology and functionality in elliptocytosis. *Biomolecules*. <https://doi.org/10.3390/biom10081120> (Epub 2020/08/06. PubMed PMID: 32751168; PubMed Central PMCID: PMCPMC7465299)
- Conrard L, Stommen A, Cloos AS, Steinkuhler J, Dimova R, Pollet H et al (2018) Spatial relationship and functional relevance of three lipid domain populations at the erythrocyte surface. *Cell Physiol Biochem* 51(4):1544–1565. <https://doi.org/10.1159/000495645> (Epub 2018/11/30. PubMed PMID: 30497064)
- Dumitru AC, Mohammed D, Maja M, Yang J, Verstraeten S, Del Campo A et al (2020) Label-free imaging of cholesterol assemblies reveals hidden nanomechanics of breast cancer cells. *Adv*

- Sci (Weinh) 7(22):2002643. <https://doi.org/10.1002/adv.202002643> (Epub 2020/11/27. PubMed PMID: 33240781; PubMed Central PMCID: PMCPMC7675049)
24. Imbalzano KM, Tatarikova I, Imbalzano AN, Nickerson JA (2009) Increasingly transformed MCF-10A cells have a progressively tumor-like phenotype in three-dimensional basement membrane culture. *Cancer Cell Int* 9:7. <https://doi.org/10.1186/1475-2867-9-7> (Epub 2009/03/18. PubMed PMID: 19291318; PubMed Central PMCID: PMCPMC2666639)
 25. Olivier M, Eeles R, Hollstein M, Khan MA, Harris CC, Hainaut P (2002) The IARC TP53 database: new online mutation analysis and recommendations to users. *Hum Mutat* 19(6):607–614. <https://doi.org/10.1002/humu.10081> (Epub 2002/05/15. PubMed PMID: 12007217)
 26. Mizuno H, Abe M, Dedecker P, Makino A, Rocha S, Ohno-Iwashita Y et al (2011) Fluorescent probes for superresolution imaging of lipid domains on the plasma membrane. *Chem Sci* 2(8):1548–1553. <https://doi.org/10.1039/C1SC00169H>
 27. Alsteens D, Newton R, Schubert R, Martinez-Martin D, Delguste M, Roska B et al (2017) Nanomechanical mapping of first binding steps of a virus to animal cells. *Nat Nanotechnol* 12(2):177–183. <https://doi.org/10.1038/nnano.2016.228> (Epub 2016/11/01. PubMed PMID: 27798607)
 28. Butt HJ, Jaschke M (1995) Calculation of thermal noise in atomic force microscopy. *Nanotechnology* 6(1):1–7. <https://doi.org/10.1088/0957-4484/6/1/001>
 29. Horzum U, Ozdil B, Pesen-Okvur D (2014) Step-by-step quantitative analysis of focal adhesions. *MethodsX* 1:56–59. <https://doi.org/10.1016/j.mex.2014.06.004> (Epub 2014/01/01. PubMed PMID: 26150935; PubMed Central PMCID: PMCPMC4472847)
 30. Martin KH, Hayes KE, Walk EL, Ammer AG, Markwell SM, Weed SA (2012) Quantitative measurement of invadopodia-mediated extracellular matrix proteolysis in single and multicellular contexts. *J Vis Exp* 66:e4119. <https://doi.org/10.3791/4119> (Epub 2012/09/07. PubMed PMID: 22952016; PubMed Central PMCID: PMCPMC3606055)
 31. Carquin M, D'Auria L, Pollet H, Bongarzone ER, Tyteca D (2016) Recent progress on lipid lateral heterogeneity in plasma membranes: From rafts to submicrometric domains. *Prog Lipid Res* 62:1–24. <https://doi.org/10.1016/j.plipres.2015.12.004> (Epub 2016/01/08. PubMed PMID: 26738447; PubMed Central PMCID: PMCPMC4851880)
 32. Arashiki N, Saito M, Koshino I, Kamata K, Hale J, Mohandas N et al (2016) An unrecognized function of cholesterol: regulating the mechanism controlling membrane phospholipid asymmetry. *Biochemistry* 55(25):3504–3513. <https://doi.org/10.1021/acs.biochem.6b00407> (Epub 2016/06/09. PubMed PMID: 27267274; PubMed Central PMCID: PMCPMC5288641)
 33. Maxfield FR, Wustner D (2012) Analysis of cholesterol trafficking with fluorescent probes. *Methods Cell Biol* 108:367–393. <https://doi.org/10.1016/B978-0-12-386487-1.00017-1> (Epub 2012/02/14. PubMed PMID: 22325611; PubMed Central PMCID: PMCPMC3626500)
 34. Hölttä-Vuori M, Uronen RL, Repakova J, Salonen E, Vattulainen I, Panula P et al (2008) BODIPY-cholesterol: a new tool to visualize sterol trafficking in living cells and organisms. *Traffic* 9(11):1839–1849. <https://doi.org/10.1111/j.1600-0854.2008.00801.x> (Epub 2008/07/24. PubMed PMID: 18647169)
 35. Marks DL, Bittman R, Pagano RE (2008) Use of Bodipy-labeled sphingolipid and cholesterol analogs to examine membrane microdomains in cells. *Histochem Cell Biol* 130(5):819–832. <https://doi.org/10.1007/s00418-008-0509-5> (Epub 2008/09/30. PubMed PMID: 18820942; PubMed Central PMCID: PMCPMC3922293)
 36. Pedersen NM, Wenzel EM, Wang L, Antoine S, Chavrier P, Stenmark H et al (2020) Protrudin-mediated ER-endosome contact sites promote MT1-MMP exocytosis and cell invasion. *J Cell Biol*. <https://doi.org/10.1083/jcb.202003063> (Epub 2020/06/02. PubMed PMID: 32479595; PubMed Central PMCID: PMCPMC7401796)
 37. Marek M, Vincenzetti V, Martin SG (2020) Sterol biosensor reveals LAM-family Ltc1-dependent sterol flow to endosomes upon Arp2/3 inhibition. *J Cell Biol*. <https://doi.org/10.1083/jcb.202001147> (Epub 2020/04/23. PubMed PMID: 32320462; PubMed Central PMCID: PMCPMC7265315)
 38. Rizzuto R, De Stefani D, Raffaello A, Mammucari C (2012) Mitochondria as sensors and regulators of calcium signalling. *Nat Rev Mol Cell Biol* 13(9):566–578. <https://doi.org/10.1038/nrm3412> (Epub 2012/08/02. PubMed PMID: 22850819)
 39. Sarmiento-Salinas FL, Delgado-Magallon A, Montes-Alvarado JB, Ramirez-Ramirez D, Flores-Alonso JC, Cortes-Hernandez P et al (2019) Breast cancer subtypes present a differential production of reactive oxygen species (ROS) and susceptibility to antioxidant treatment. *Front Oncol* 9:480. <https://doi.org/10.3389/fonc.2019.00480> (Epub 2019/06/25. PubMed PMID: 31231612; PubMed Central PMCID: PMCPMC6568240)
 40. Giacomini I, Gianfanti F, Desbats MA, Orso G, Berretta M, Prayer-Galetti T et al (2021) Cholesterol metabolic reprogramming in cancer and its pharmacological modulation as therapeutic strategy. *Front Oncol* 11:682911. <https://doi.org/10.3389/fonc.2021.682911> (Epub 2021/06/11. PubMed PMID: 34109128; PubMed Central PMCID: PMCPMC8181394)
 41. Yang Z, Qin W, Chen Y, Yuan B, Song X, Wang B et al (2018) Cholesterol inhibits hepatocellular carcinoma invasion and metastasis by promoting CD44 localization in lipid rafts. *Cancer Lett* 429:66–77. <https://doi.org/10.1016/j.canlet.2018.04.038> (Epub 2018/05/11. PubMed PMID: 29746928)
 42. Zhang J, Li Q, Wu Y, Wang D, Xu L, Zhang Y et al (2019) Cholesterol content in cell membrane maintains surface levels of ErbB2 and confers a therapeutic vulnerability in ErbB2-positive breast cancer. *Cell Commun Signal* 17(1):15. <https://doi.org/10.1186/s12964-019-0328-4> (Epub 2019/02/23. PubMed PMID: 30786890; PubMed Central PMCID: PMCPMC6383291)
 43. Zhao Z, Hao D, Wang L, Li J, Meng Y, Li P et al (2019) CtBP promotes metastasis of breast cancer through repressing cholesterol and activating TGF-beta signaling. *Oncogene* 38(12):2076–2091. <https://doi.org/10.1038/s41388-018-0570-z> (Epub 2018/11/18. PubMed PMID: 30442980)
 44. Das A, Brown MS, Anderson DD, Goldstein JL, Radhakrishnan A (2014) Three pools of plasma membrane cholesterol and their relation to cholesterol homeostasis. *Elife*. <https://doi.org/10.7554/eLife.02882> (Epub 2014/06/13. PubMed PMID: 24920391; PubMed Central PMCID: PMCPMC4086274)
 45. Wang H, Ma Q, Qi Y, Dong J, Du X, Rae J et al (2019) ORP2 Delivers cholesterol to the plasma membrane in exchange for phosphatidylinositol 4, 5-bisphosphate (PI(4,5)P2). *Mol Cell* 73(3):458–73 e7. <https://doi.org/10.1016/j.molcel.2018.11.014> (Epub 2018/12/26. PubMed PMID: 30581148)
 46. Kentala H, Koponen A, Kivela AM, Andrews R, Li C, Zhou Y et al (2018) Analysis of ORP2-knockout hepatocytes uncovers a novel function in actin cytoskeletal regulation. *FASEB J* 32(3):1281–1295. <https://doi.org/10.1096/fj.201700604R> (Epub 2017/11/03. PubMed PMID: 29092904)
 47. Prinz WA (2014) Bridging the gap: membrane contact sites in signaling, metabolism, and organelle dynamics. *J Cell Biol* 205(6):759–769. <https://doi.org/10.1083/jcb.201401126> (Epub 2014/06/25. PubMed PMID: 24958771; PubMed Central PMCID: PMCPMC4068136)

48. Gil-Hernandez A, Arroyo-Campuzano M, Simoni-Nieves A, Zazueta C, Gomez-Quiroz LE, Silva-Palacios A (2020) Relevance of membrane contact sites in cancer progression. *Front Cell Dev Biol* 8:622215. <https://doi.org/10.3389/fcell.2020.622215> (Epub 2021/01/30. PubMed PMID: 33511135; PubMed Central PMCID: PMCPCMC7835521)
49. Sandhu J, Li S, Fairall L, Pfisterer SG, Gurnett JE, Xiao X et al (2018) Aster proteins facilitate nonvesicular plasma membrane to ER cholesterol transport in mammalian cells. *Cell* 175(2):514–529 e20. <https://doi.org/10.1016/j.cell.2018.08.033> (Epub 2018/09/18. PubMed PMID: 30220461; PubMed Central PMCID: PMCPCMC6469685)
50. Naito T, Ercan B, Krshnan L, Triebel A, Koh DHZ, Wei FY et al (2019) Movement of accessible plasma membrane cholesterol by the GRAMD1 lipid transfer protein complex. *Elife*. <https://doi.org/10.7554/eLife.51401> (Epub 2019/11/15. PubMed PMID: 31724953; PubMed Central PMCID: PMCPCMC6905856)
51. Wu H, Carvalho P, Voeltz GK (2018) Here, there, and everywhere: the importance of ER membrane contact sites. *Science*. <https://doi.org/10.1126/science.aan5835> (Epub 2018/08/04. PubMed PMID: 30072511; PubMed Central PMCID: PMCPCMC6568312)
52. Menon AK (2018) Sterol gradients in cells. *Curr Opin Cell Biol* 53:37–43. <https://doi.org/10.1016/j.ceb.2018.04.012> (PubMed PMID: 29783105)
53. Guerra FS, Sampaio LDS, Konig S, Bonamino M, Rossi MID, Costa ML et al (2016) Membrane cholesterol depletion reduces breast tumor cell migration by a mechanism that involves non-canonical Wnt signaling and IL-10 secretion. *Transl Med Commun* 1(1):3. <https://doi.org/10.1186/s41231-016-0002-4>
54. Kumar M, Irungbam K, Kataria M (2018) Depletion of membrane cholesterol compromised caspase-8 imparts in autophagy induction and inhibition of cell migration in cancer cells. *Cancer Cell Int* 18:23. <https://doi.org/10.1186/s12935-018-0520-4> (Epub 2018/02/23. PubMed PMID: 29467593; PubMed Central PMCID: PMCPCMC5819249)
55. Liu Z, Liu X, Liu S, Cao Q (2018) Cholesterol promotes the migration and invasion of renal carcinoma cells by regulating the KLF5/miR-27a/FBXW7 pathway. *Biochem Biophys Res Commun* 502(1):69–75. <https://doi.org/10.1016/j.bbrc.2018.05.122> (Epub 2018/05/22. PubMed PMID: 29782853)
56. Caldieri G, Giacchetti G, Beznoussenko G, Attanasio F, Ayala I, Buccione R (2009) Invadopodia biogenesis is regulated by caveolin-mediated modulation of membrane cholesterol levels. *J Cell Mol Med* 13(8B):1728–1740. <https://doi.org/10.1111/j.1582-4934.2008.00568.x> (Epub 2009/01/30. PubMed PMID: 19175685; PubMed Central PMCID: PMCPCMC6512369)
57. Yamaguchi H, Takeo Y, Yoshida S, Kouchi Z, Nakamura Y, Fukami K (2009) Lipid rafts and caveolin-1 are required for invadopodia formation and extracellular matrix degradation by human breast cancer cells. *Cancer Res* 69(22):8594–8602. <https://doi.org/10.1158/0008-5472.CAN-09-2305> (Epub 2009/11/06. PubMed PMID: 19887621)
58. Yang H, Guan L, Li S, Jiang Y, Xiong N, Li L et al (2016) Mechanosensitive caveolin-1 activation-induced PI3K/Akt/mTOR signaling pathway promotes breast cancer motility, invadopodia formation and metastasis in vivo. *Oncotarget* 7(13):16227–16247. <https://doi.org/10.18632/oncotarget.7583> (Epub 2016/02/27. PubMed PMID: 26919102; PubMed Central PMCID: PMCPCMC4941310)
59. Poincloux R, Lizarraga F, Chavrier P (2009) Matrix invasion by tumour cells: a focus on MT1-MMP trafficking to invadopodia. *J Cell Sci* 122(Pt 17):3015–3024. <https://doi.org/10.1242/jcs.034561> (Epub 2009/08/21. PubMed PMID: 19692588)
60. Artym VV, Zhang Y, Seillier-Moisewitsch F, Yamada KM, Mueller SC (2006) Dynamic interactions of cortactin and membrane type 1 matrix metalloproteinase at invadopodia: defining the stages of invadopodia formation and function. *Cancer Res* 66(6):3034–3043. <https://doi.org/10.1158/0008-5472.CAN-05-2177> (Epub 2006/03/17. PubMed PMID: 16540652)
61. Hoshino D, Branch KM, Weaver AM (2013) Signaling inputs to invadopodia and podosomes. *J Cell Sci* 126(Pt 14):2979–2989. <https://doi.org/10.1242/jcs.079475> (Epub 2013/07/12. PubMed PMID: 23843616; PubMed Central PMCID: PMCPCMC3711196)
62. Lin CY, Huang JY, Lo LW (2016) Exploring in vivo cholesterol-mediated interactions between activated EGF receptors in plasma membrane with single-molecule optical tracking. *BMC Biophys* 9:6. <https://doi.org/10.1186/s13628-016-0030-5> (Epub 2016/06/28. PubMed PMID: 27347397; PubMed Central PMCID: PMCPCMC4919887)
63. Zhuang L, Lin J, Lu ML, Solomon KR, Freeman MR (2002) Cholesterol-rich lipid rafts mediate akt-regulated survival in prostate cancer cells. *Cancer Res* 62(8):2227–2231 (Epub 2002/04/17. PubMed PMID: 11956073)
64. Bag N, Huang S, Wohland T (2015) Plasma membrane organization of epidermal growth factor receptor in resting and ligand-bound states. *Biophys J* 109(9):1925–1936. <https://doi.org/10.1016/j.bpj.2015.09.007> (Epub 2015/11/05. PubMed PMID: 26536269; PubMed Central PMCID: PMCPCMC4643207)
65. Moss NM, Liu Y, Johnson JJ, Debiase P, Jones J, Hudson LG et al (2009) Epidermal growth factor receptor-mediated membrane type 1 matrix metalloproteinase endocytosis regulates the transition between invasive versus expansive growth of ovarian carcinoma cells in three-dimensional collagen. *Mol Cancer Res* 7(6):809–820. <https://doi.org/10.1158/1541-7786.MCR-08-0571> (Epub 2009/06/11. PubMed PMID: 19509114; PubMed Central PMCID: PMCPCMC2843416)
66. Itoh Y (2015) Membrane-type matrix metalloproteinases: their functions and regulations. *Matrix Biol* 44–46:207–223. <https://doi.org/10.1016/j.matbio.2015.03.004> (Epub 2015/03/22. PubMed PMID: 25794647)
67. Quon E, Sere YY, Chauhan N, Johansen J, Sullivan DP, Dittman JS et al (2018) Endoplasmic reticulum-plasma membrane contact sites integrate sterol and phospholipid regulation. *PLoS Biol* 16(5):e2003864. <https://doi.org/10.1371/journal.pbio.2003864> (Epub 2018/05/22. PubMed PMID: 29782498; PubMed Central PMCID: PMCPCMC5983861)
68. Lu M, van Tartwijk FW, Lin JQ, Nijenhuis W, Parutto P, Fantam M et al (2020) The structure and global distribution of the endoplasmic reticulum network are actively regulated by lysosomes. *Sci Adv*. <https://doi.org/10.1126/sciadv.abc7209> (Epub 2020/12/18. PubMed PMID: 33328230; PubMed Central PMCID: PMCPCMC7744115)
69. Kanerva K, Uronen RL, Blom T, Li S, Bittman R, Lappalainen P et al (2013) LDL cholesterol recycles to the plasma membrane via a Rab8a-Myosin5b-actin-dependent membrane transport route. *Dev Cell* 27(3):249–262. <https://doi.org/10.1016/j.devcel.2013.09.016> (Epub 2013/11/12. PubMed PMID: 24209575)

Supporting Information

Surface cholesterol-enriched domains specifically promote invasion of breast cancer cell lines by controlling invadopodia and extracellular matrix degradation

Mauriane Maja¹, Danahe Mohammed², Andra C. Dumitru², Sandrine Verstraeten³, Maxime Lingurski¹, Marie-Paule Mingeot-Leclercq³, David Alsteens², Donatienne Tyteca^{1}*

¹CELL Unit and PICT Imaging Platform, de Duve Institute, UCLouvain, Brussels, Belgium

²Louvain Institute of Biomolecular Science and Technology (LIBST), UCLouvain, Ottignies-Louvain-la-Neuve, Belgium

³Cellular and Molecular Pharmacology Unit (FACM), Louvain Drug Research Institute, UCLouvain, Brussels, Belgium

***Corresponding author:** Donatienne Tyteca, CELL Unit, de Duve Institute, UCLouvain, B1.75.05, avenue Hippocrate, 75, B-1200 Brussels, Belgium. Phone: +32-2-764.75.91; Fax: +32-2-764.75.43; e-mail: donatienne.tyteca@uclouvain.be

Materials and Methods

Western blotting. Cells were washed in PBS, lysed in cold RIPA lysis buffer (150 mM NaCl, 0.5% sodium deoxycholate, 50 mM Tris, 0.1% SDS, 1% Triton X-100, 1 mM PMSF, cOmplete™ Protease Inhibitor Cocktail) for 25 min, then sonicated for 15 sec. Red blood cell ghosts were used as negative control and prepared as previously described [1, 2]. Cell lysates were mixed in 2% sample buffer (0.25 M Tris-HCl, pH 6.8, 10% SDS, 20% glycerol, 0.005% bromophenol blue) containing 5 mM Dithiothreitol (DTT) or not, and boiled for 5 min. Western blotting was performed as previously [3], except that samples were loaded on 3-10% SDS-PAGE gel.

Thin Layer Chromatography. Cells were treated with mβCD then washed in PBS. To lyse the cells, the cell suspension was diluted at 1×10^6 cell/mL in 0.9% NaCl then submitted to 2 cycles of freezing/thawing at -80 °C and vortexed. To extract all lipids, 3 mL of ice-cold chloroform/methanol (2:1; v/v) was added to 1 mL of cell lysate. The solution was vortexed and centrifuged for 15 min at 3000 rpm at room temperature. The organic phase was evaporated and resuspended in 80 μL chloroform/methanol, separated by thin layer chromatography (TLC) in chloroform:methanol:15mM CaCl₂ (65:35:8; v/v/v) and revealed by charring densitometry after staining with 10% cupric sulfate in 8% O-phosphoric acid. Lipids were identified with the standards and phosphatidylethanolamine (PE), phosphatidylcholine (PC), 1,2-dioleoyl-sn-glycero-3-phosphocholine (DOPC) and sphingomyelin (SM) band intensity was quantified using ImageJ/Fiji and expressed by reference to the sum of all band intensities.

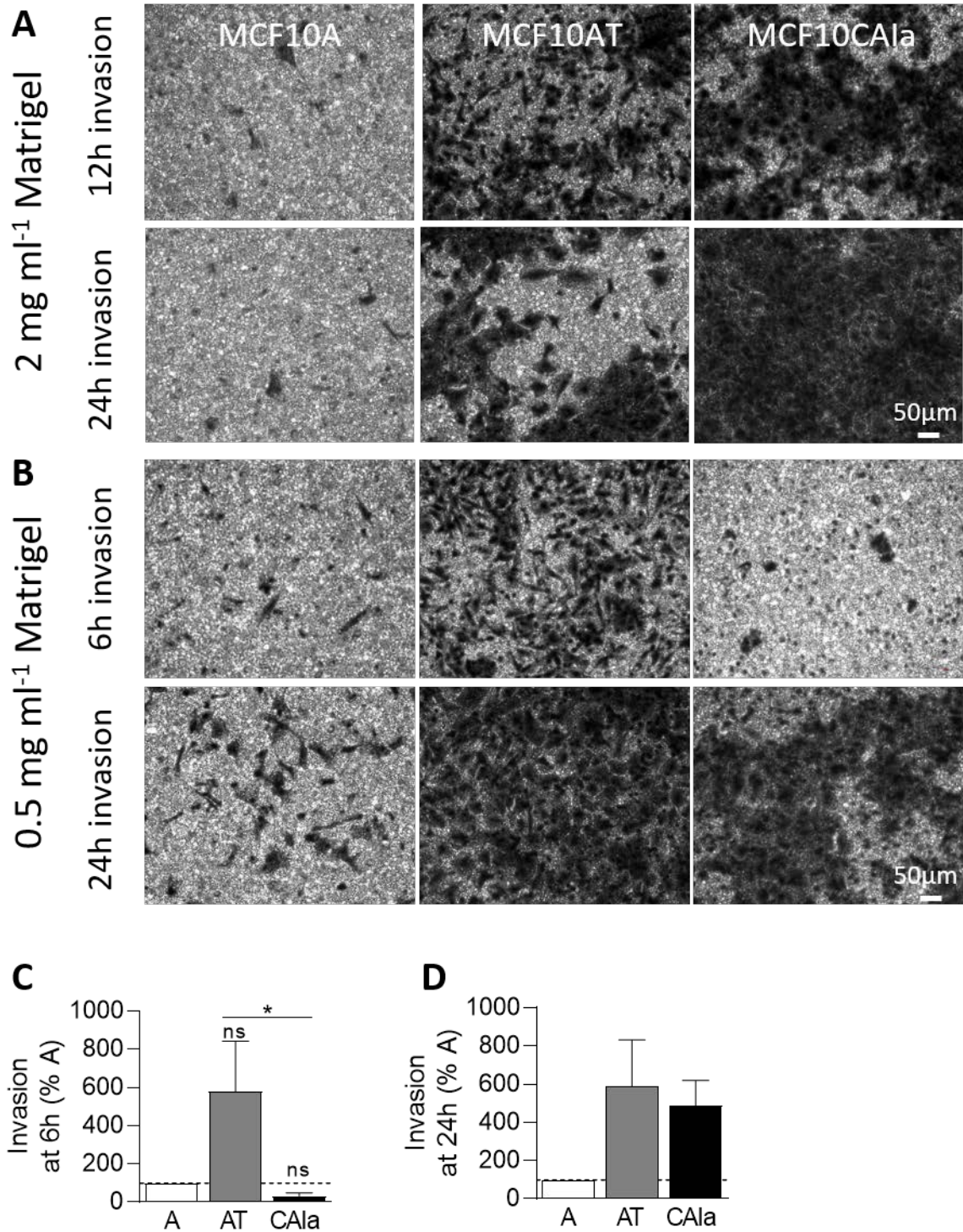


Fig. S1 Effect of time and Matrigel concentration on invasion of the MCF10A cell line series. (A) Representative images of invasion of the 3 cell lines in Transwell with a dense (2 mg ml⁻¹) Matrigel layer toward 10% serum for 12h and 24h. (B) Representative images of cell invasion potential in Transwell with a loose (0.5 mg ml⁻¹) Matrigel layer toward 10% serum for 6h and 24h. (C-D) Quantification of invasion of the 3 cell lines in Transwell with a loose Matrigel layer toward 10% serum for 6h (C; n=3-4 Transwell from 4 independent experiments) or 24h (D; n=2 Transwell from 1 experiment). Kruskal-Wallis test followed by Dunn's comparison test

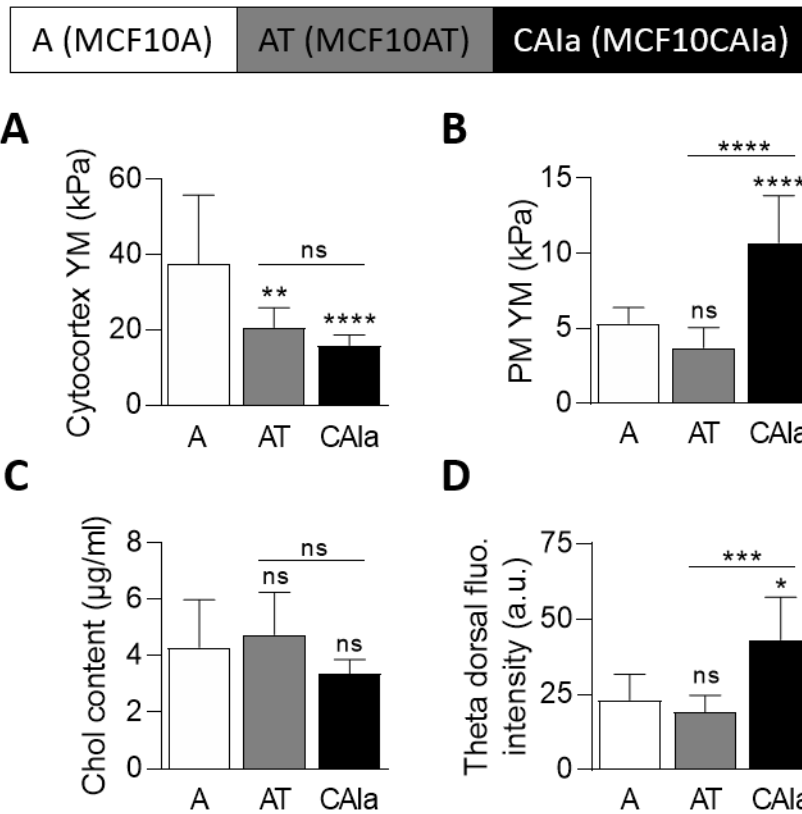


Fig. S2 The MCF10A cell lines series exhibits differential extents of cytocortex and [PM-plasma membrane](#) stiffness, chol content and chol surface distribution. (A,B) Cytocortex (A) and PM (B) Young's modulus of the 3 cell lines determined by AFM. Reproduced with permission [4] Copyright 2020, Advanced Science. (C) Total free chol content of the 3 cell lines assessed by Amplex Red assay (n=7-9 independent experiments). (D) Quantification of the Theta dorsal fluorescence intensity of the 3 cell lines plated on glass coverslips and labeled at 4 °C with the mCherry-Theta toxin fragment (4-10 cells from n=4-28 images from 3-8 independent experiments). Kruskal-Wallis test followed by Dunn's comparison test.

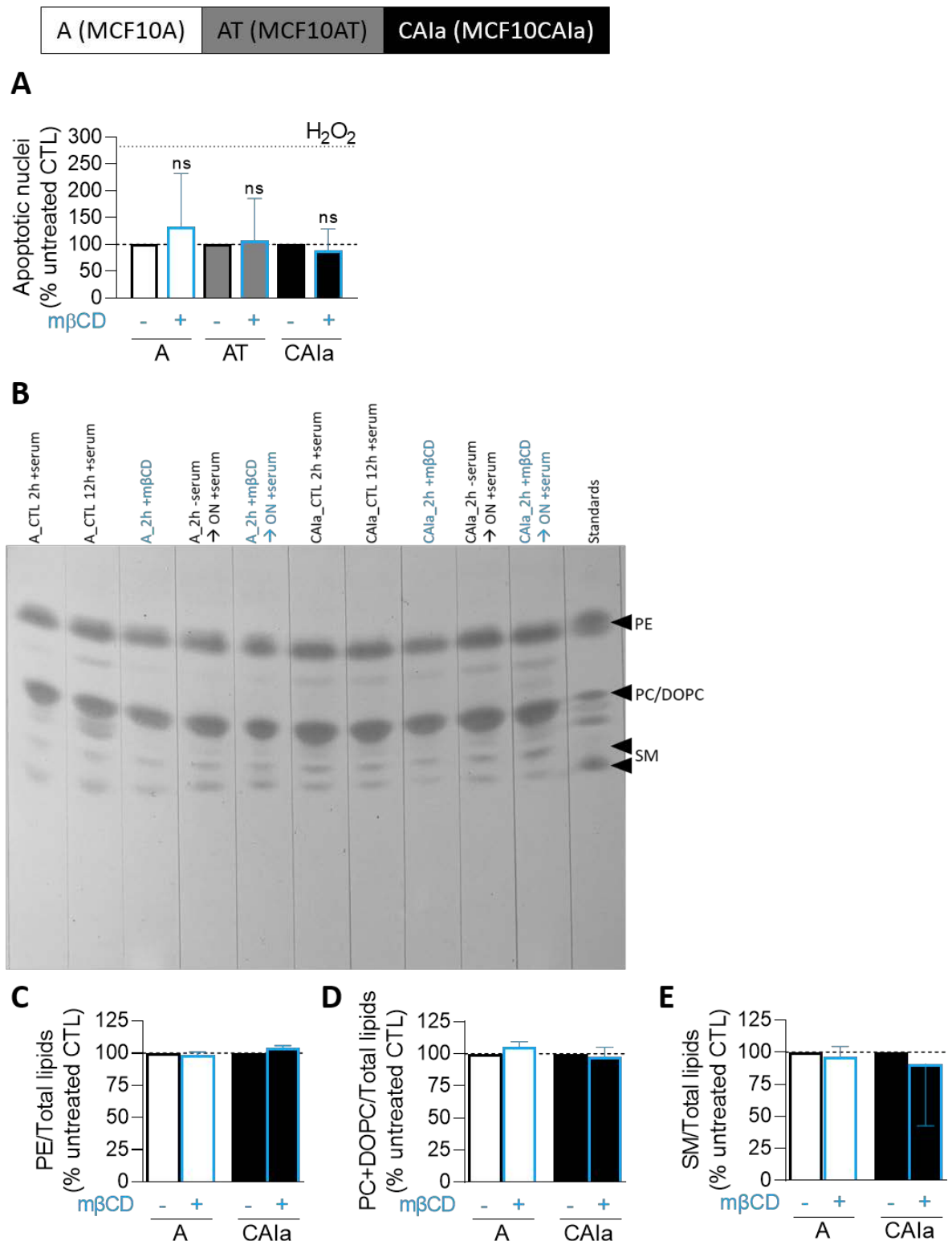


Fig. S3 Cholesterol depletion by 2 mM methyl- β -cyclodextrin treatment does not induce apoptosis and does not extract sphingo- and phospholipids. (A) Quantification of the proportion of apoptotic nuclei in the 3 cell lines plated on glass coverslips, treated or not (-, black) with 2 mM m β CD for 2h (+, blue) then labeled with DAPI, visualized by confocal microscopy and quantified (n=1026-2418 nuclei from 3 independent experiments). Horizontal dotted line, 10 mM hydrogen peroxide (H₂O₂) used as positive control. Unpaired t test. (B-E) Thin layer chromatography on A and CAIa cell lysates. All cells were serum-starved for 2h, combined or not (black

conditions) with 2 mM m β CD (blue conditions), then stimulated or not overnight (ON) with serum-containing medium. (B) Representative image. Arrowheads show the positions of phosphatidylethanolamine (PE), phosphatidylcholine (PC), 1,2-dioleoyl-sn-glycero-3-phosphocholine (DOPC) and sphingomyelin (SM; 2 bands) identified with the standards (n=1 experiment). (C-E) Quantification of PE (C), PC+DOPC (D) and SM (E) abundance in A and CA1a lysates treated or not with 2 mM m β CD (blue). Data represent the mean of 2h serum starvation followed or not by ON stimulation in serum conditions (n=1 experiment)

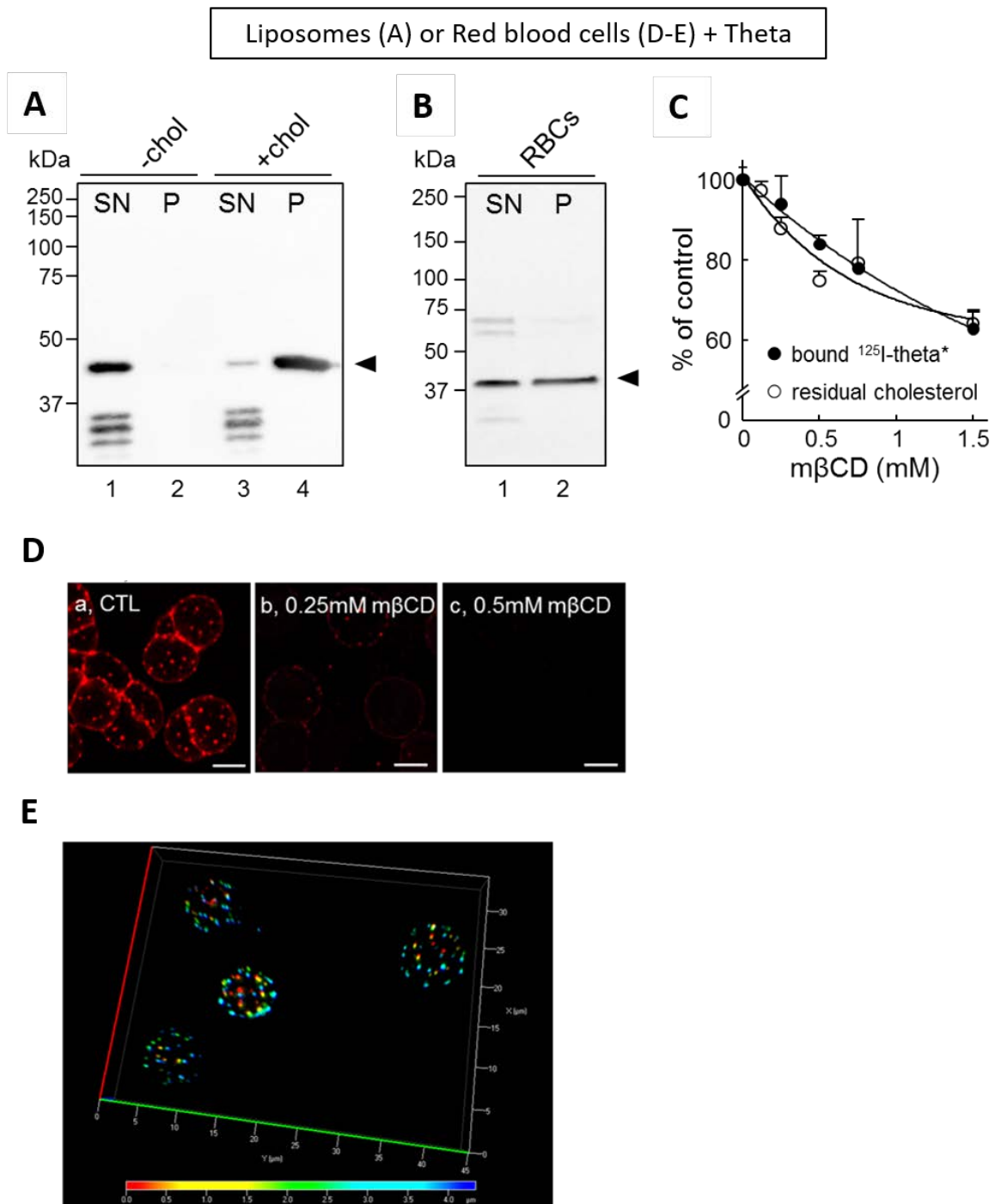


Fig. S4 The Theta toxin fragment specifically binds to cholesterol and reveals cholesterol-enriched submicrometric domains on living spread red blood cells. (A,B) Specific binding of Theta to liposomes containing chol and to red blood cells (RBCs). Theta was incubated with multilamellar vesicles (MLVs; A) containing chol (+ chol; lanes 3 and 4) or not (- chol; lanes 1 and 2), or with freshly isolated RBCs in suspension (B). After centrifugation, pellets (P) containing MLVs (A) or RBCs (B) and supernatants (SN) were analyzed by Western blotting for the His-tag on Theta. Arrowheads correspond to the expected position of intact mCherry-Theta (~41kDa). (C) Correspondence between Theta binding and chol level in RBCs. Freshly isolated RBCs were either kept untreated or chol-depleted by mβCD prior to labeling in suspension with ¹²⁵I-Theta mixed with 1μM cold Theta (in the continued presence of mβCD if appropriate). After washing by iterative centrifugation/resuspension, ¹²⁵I-Theta bound to RBCs was measured and expressed as percentage of control cells (filled circles). Decrease of Theta binding closely parallels

residual chol level (open circles). (D) Evidence for chol-enriched domains on living spread RBCs. Freshly isolated RBCs were either kept untreated (CTL; a) or chol-depleted by 0.25mM (b; - ~15% chol) or 0.5mM (c; - ~25% chol) m β CD at 37 °C, labeled in suspension with Theta in the continuous presence of m β CD, washed, attached-spread onto poly-L-lysine-coated coverslips and visualized by confocal microscopy at 20 °C. (E) Chol submicrometric domains are present on both sides of living spread RBCs. Fresh RBCs were labeled and spread and observed with wide-field fluorescence microscope. 3D-deconvolution and depth pseudo-coloration were then applied to visualize domain position in 3D (red corresponds to poly-L-lysine-free side, blue to poly-L-lysine-attached side). Adapted from [5]

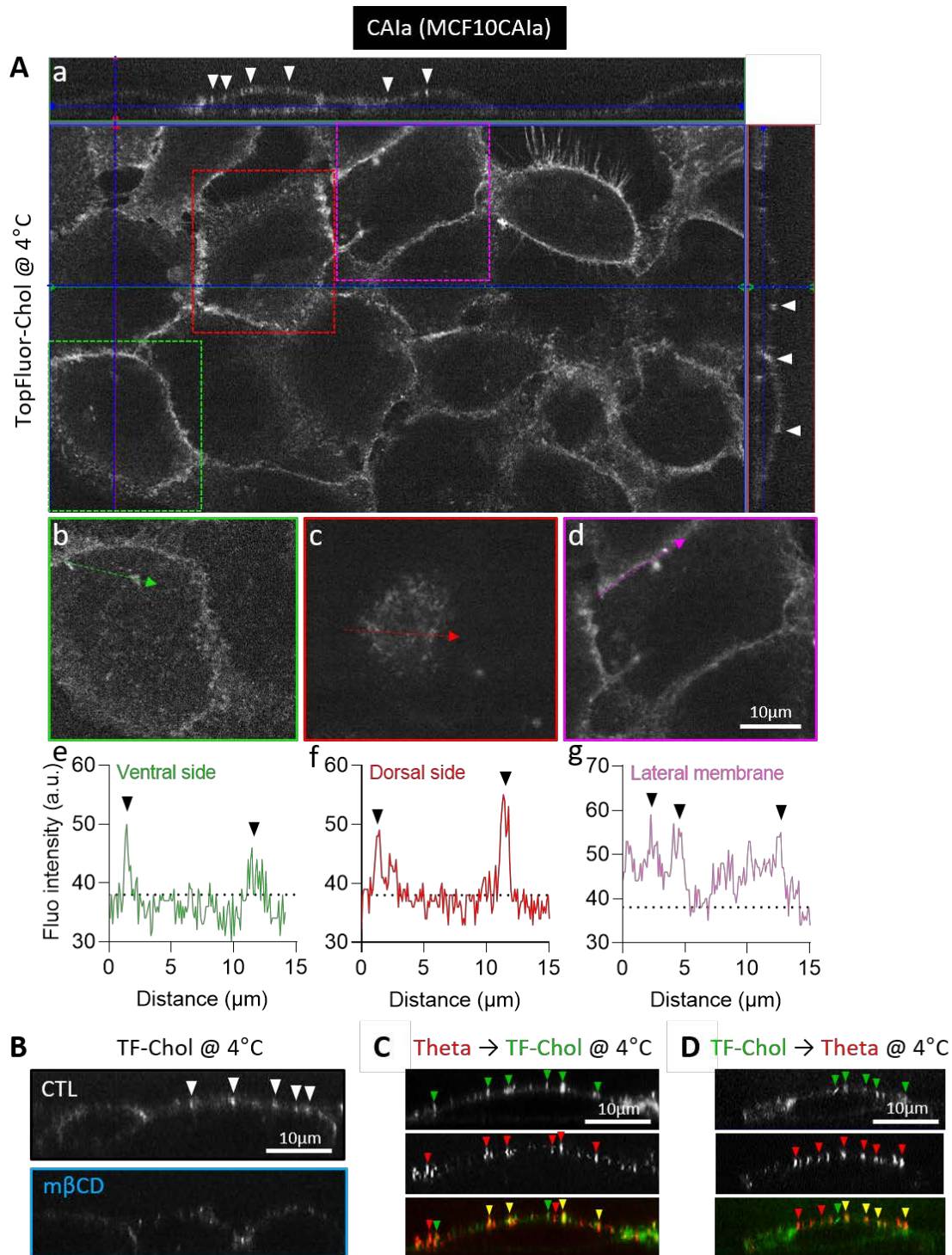


Fig. S5 Plasma membrane insertion of TopFluor-Cholesterol reveals cholesterol-enriched submicrometric domains at the dorsal face of malignant CAIa cells that are decreased by methyl-β-cyclodextrin and largely correspond to the Theta-decorated domains. CAIa cells were plated on fibronectin-coated coverslips and then tested for surface chol distribution. (A) CAIa cells labeled at 4 °C with the chol analog TopFluor-Cholesterol. a, Representative image and X-Z reconstructions along the blue lines in the X-Y section. b-g, Insets showing 3 cells at ventral (green), dorsal (red) and lateral (purple) sections respectively and the corresponding fluorescence intensity profiles along the dotted lines (n=3 experiments). Arrowheads, chol-enriched domains. (B) CAIa treated or not with 2mM mβCD for 2h (blue) and labeled at 4 °C with the TopFluor-Cholesterol (TF-Chol). X-Z

reconstructions of confocal images are shown (n=2 experiments). Arrowheads, dorsal chol-enriched domains. (C,D) CA1a cells sequentially labeled at 4 °C with the mCherry-Theta toxin fragment specific to endogenous chol then with the TopFluor-Cholesterol (C) or vice versa (D) (n=2 experiments). Arrowheads, dorsal chol-enriched domains labeled with the TopFluor-Cholesterol (green), with the mCherry-Theta toxin fragment (red) or with both probes (yellow)

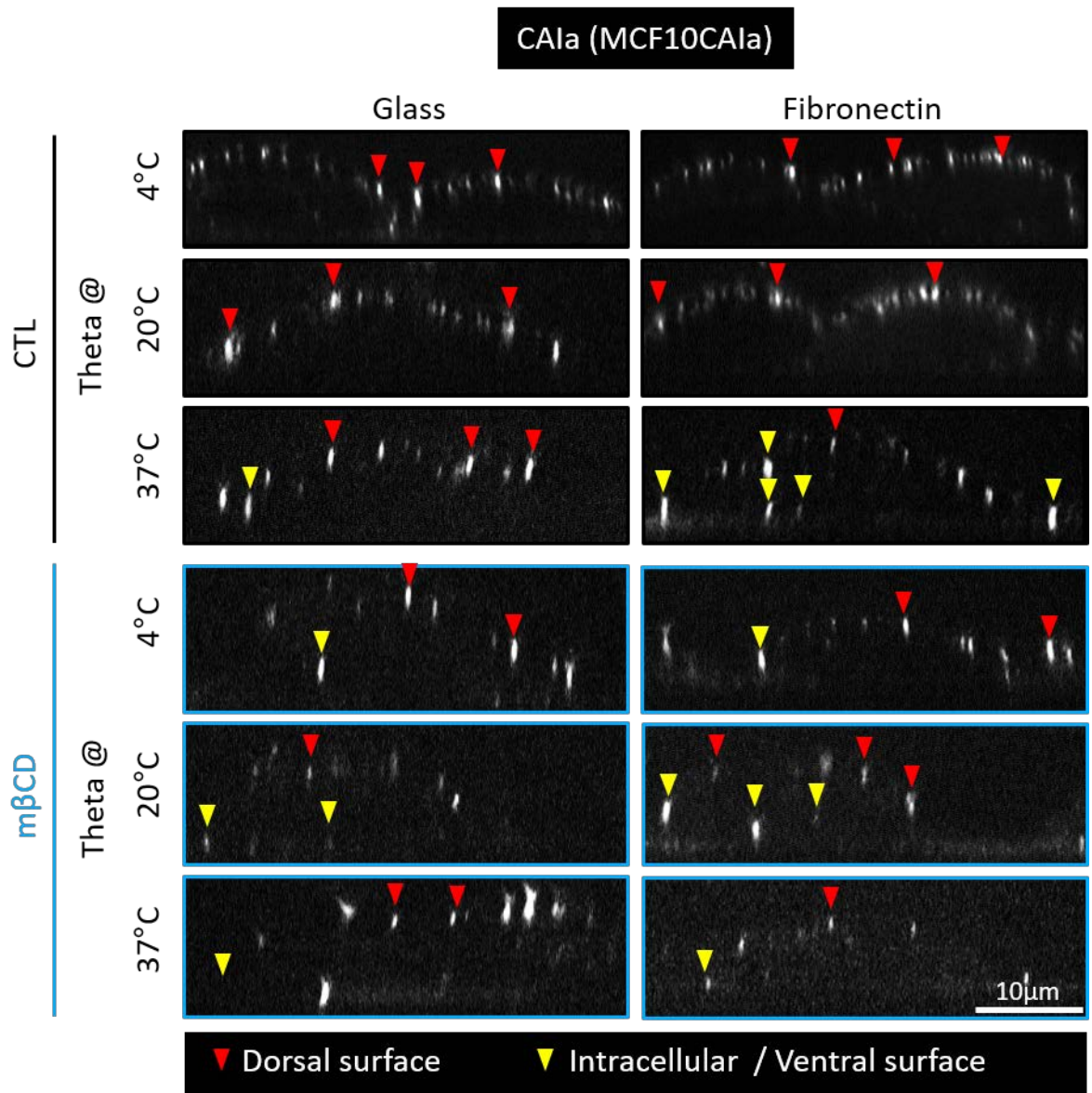


Fig. S6 Cholesterol depletion removes a dorsal surface cholesterol pool that can be internalized and reach the ventral face. MCF10CAIa were plated on glass or fibronectin-coated coverslips, treated with 2 mM mβCD for 2h (blue) and labeled at the indicated temperature with the mCherry-Theta toxin fragment as in Figure 2I. X-Z reconstructions of confocal images

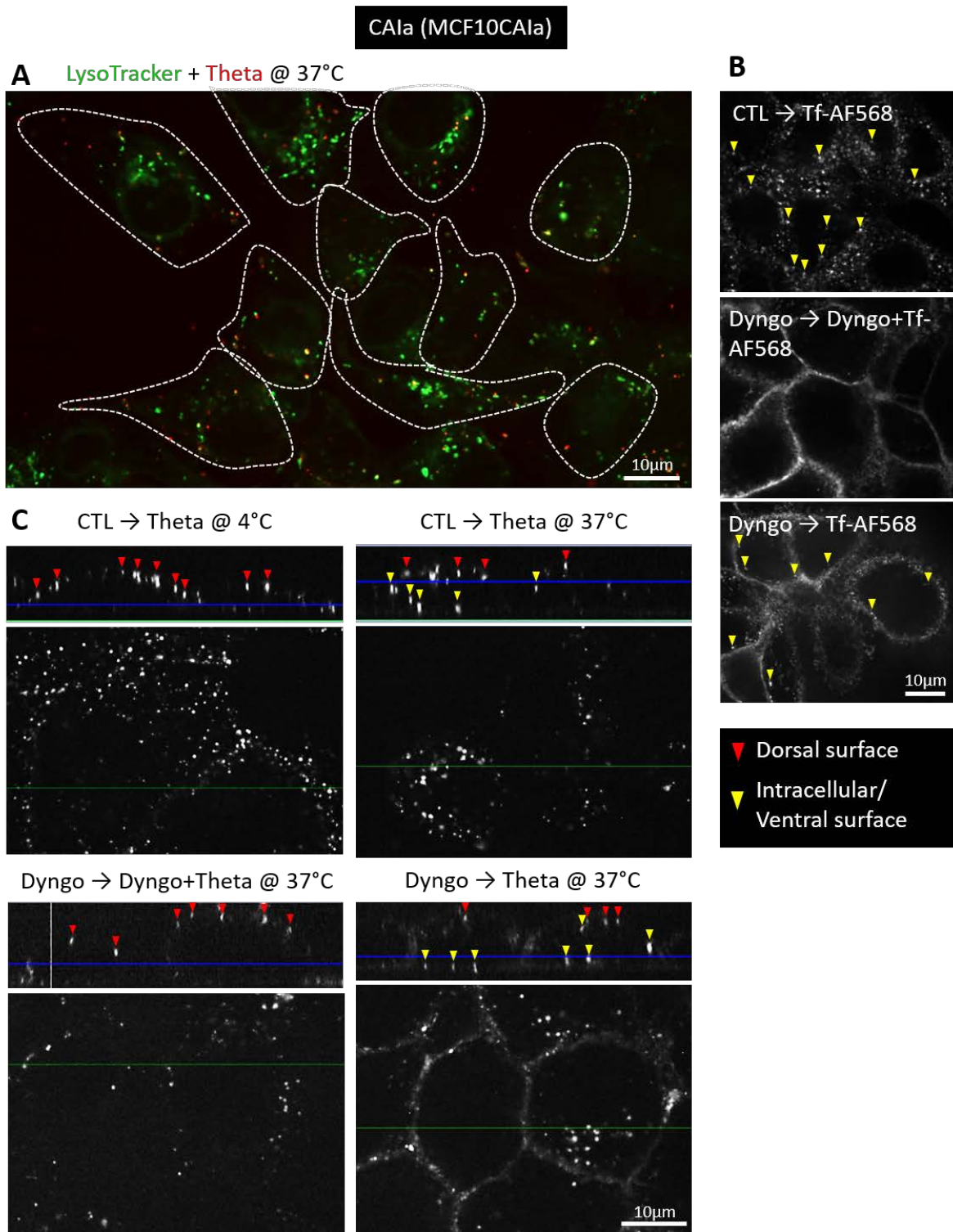


Fig. S7 Large colocalization of Theta with late endosomes/lysosomes and impairment of cholesterol-enriched domain redistribution to the ventral side upon inhibition of endocytosis in malignant CAIa cells. (A) Extension of Fig. 2J showing CAIa cells colabeled at 37 °C with the mCherry-Theta toxin fragment and the LysoTracker. (B,C) Inhibition of endocytosis in CAIa cells plated on fibronectin-coated coverslips, treated or not with 20 µM Dyngo4a, a dynamin inhibitor, then incubated at 37 °C with the Alexa568-transferrin (B; Tf-AF568 used as positive control) or with the mCherry-Theta toxin fragment (C) in the continuous presence or not of Dyngo4a and analyzed by

confocal microscopy. Red arrowheads, chol-enriched domains at the dorsal side; yellow arrowheads, chol-enriched domains or Tf-positive structures inside the cells or at ventral face

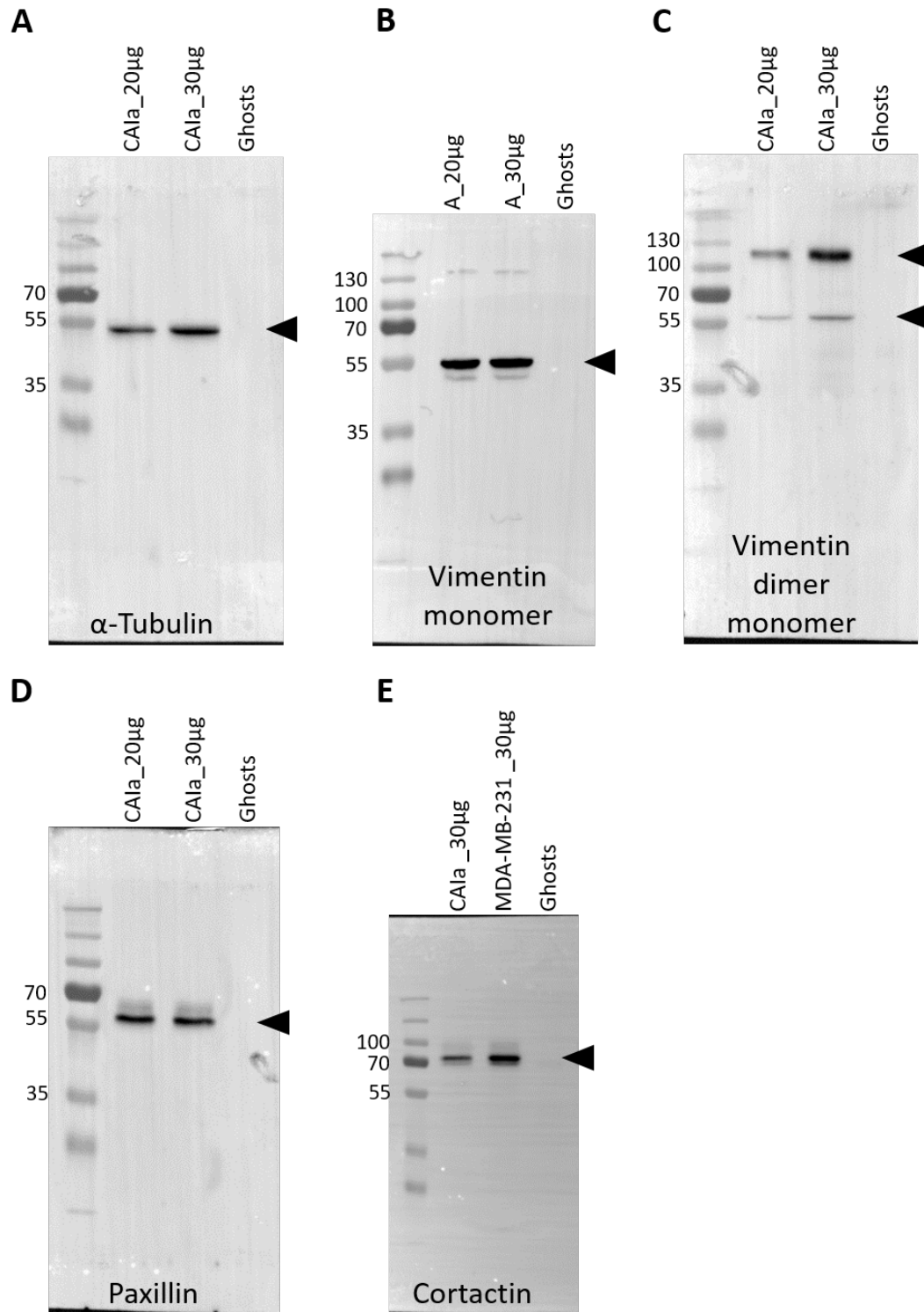


Fig. S8 Specificity of anti- α -Tubulin, -Vimentin, -Paxillin and -Cortactin antibodies. Western blottings against α -Tubulin (A), Vimentin (monomer in A and mainly dimer in CAIa cells; B and C respectively), Paxillin (D) and Cortactin (E) on CAIa (A,C,D,E) and/or MDA-MB-231 (E) cell lysates. Erythrocyte ghosts were used as negative controls

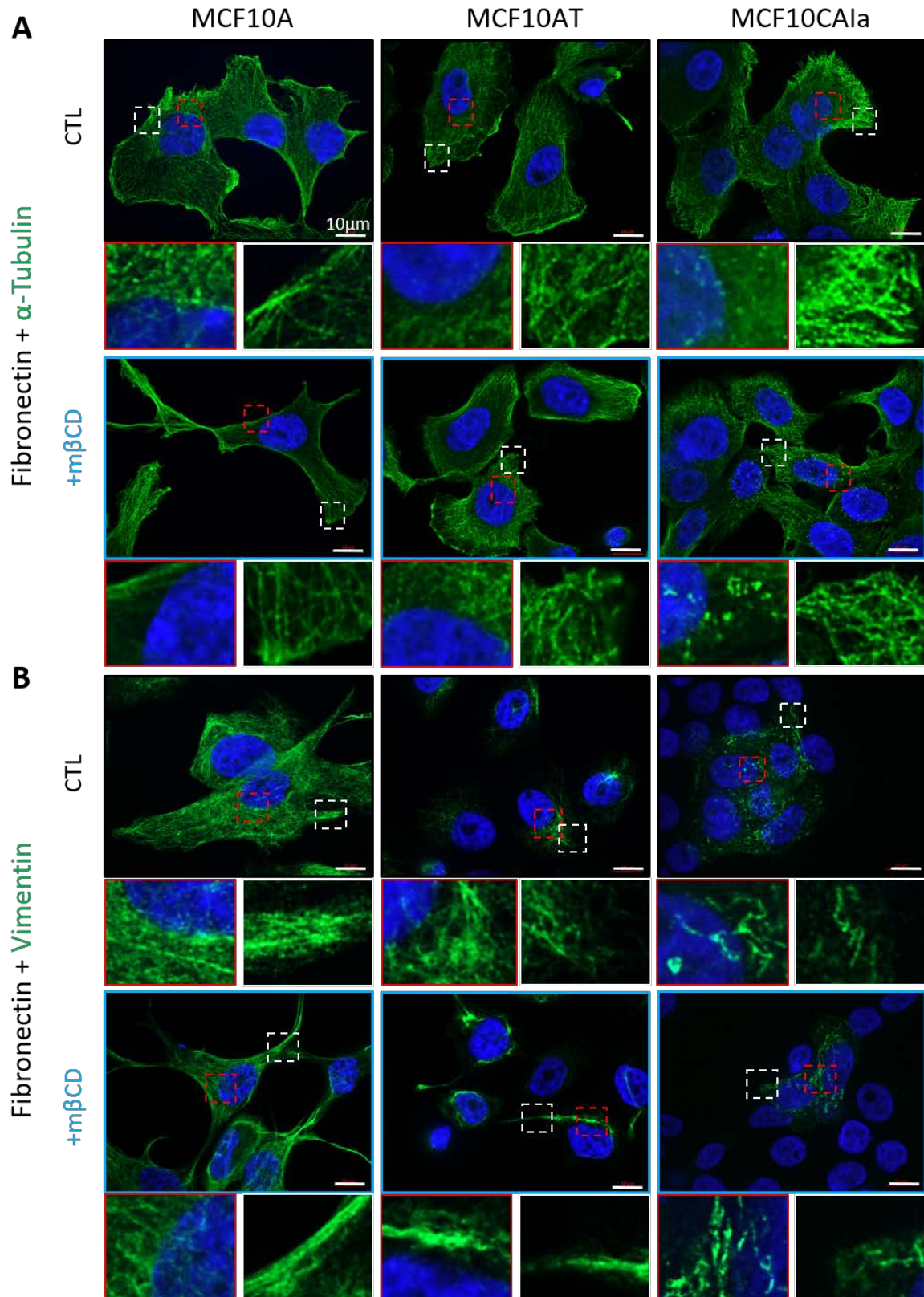


Fig. S9 Preservation of microtubule and intermediate filament distribution upon cholesterol depletion. The 3 cell lines were plated on fibronectin-coated coverslips, treated or not with 2 mM m β CD for 2h (blue), immunolabeled with anti- α -Tubulin (A) or anti-Vimentin (B) and visualized by confocal microscopy. Nuclei stained with Hoechst in blue. Red insets, perinuclear regions; White insets, peripheral regions

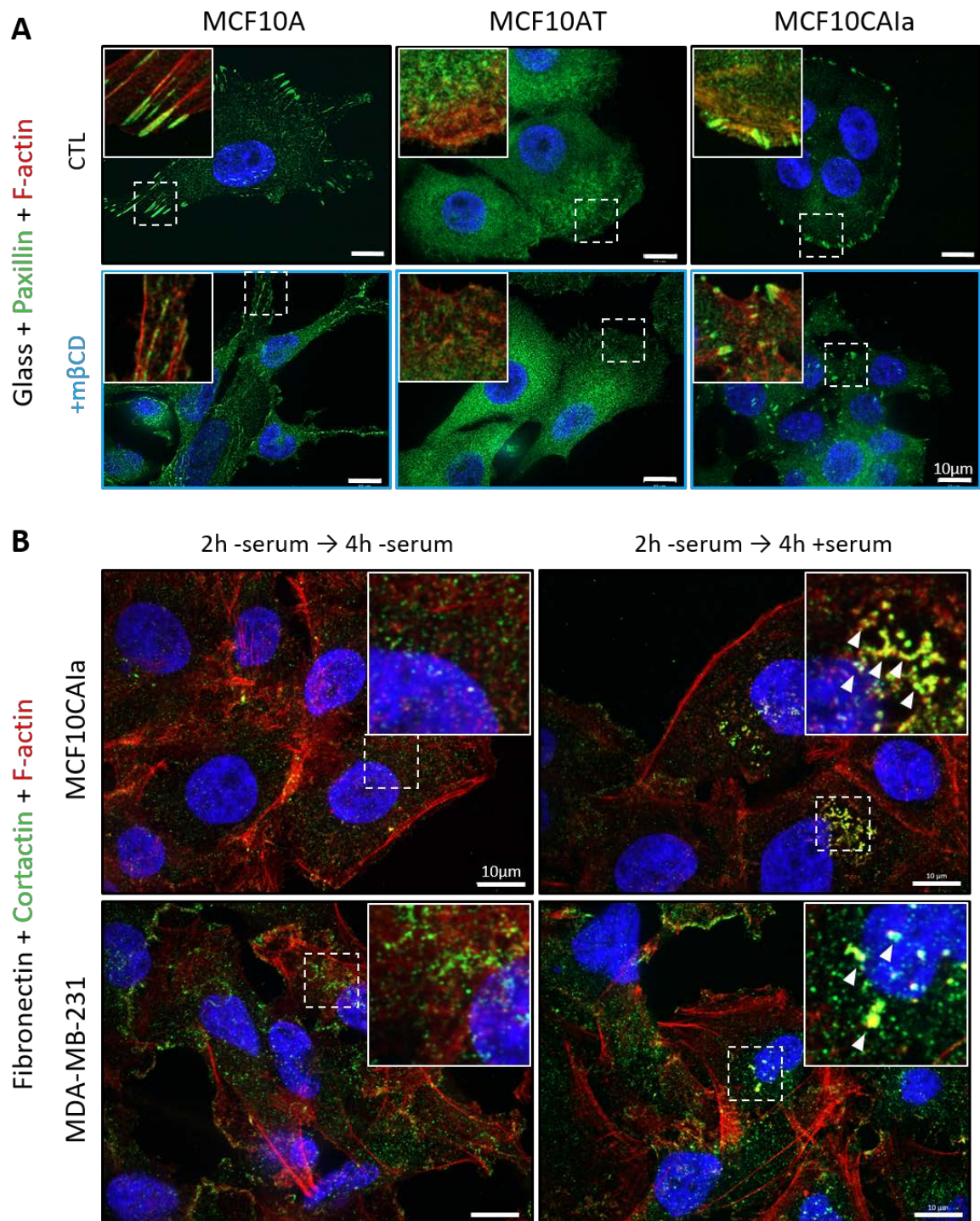


Fig. S10 Cholesterol depletion impairs focal adhesions specifically in normal cells and serum starvation followed by reincubation in serum-containing medium stimulates the formation of invadopodia. (A) Confocal images of the 3 cell lines plated on glass coverslips, treated or not with 2 mM mβCD for 2h and immunolabeled with anti-Paxillin together with F-Actin (Phalloidin) and nuclei (Hoechst). Insets show Paxillin-positive focal adhesions. (B) Confocal images of CA1a and MDA-MB-231 plated on fibronectin-coated coverslips, serum starved for 2h then stimulated 4h with serum containing medium to allow reformation of invadopodia and immunolabeled with anti-Cortactin together with F-actin (Phalloidin) and nuclei (Hoechst)

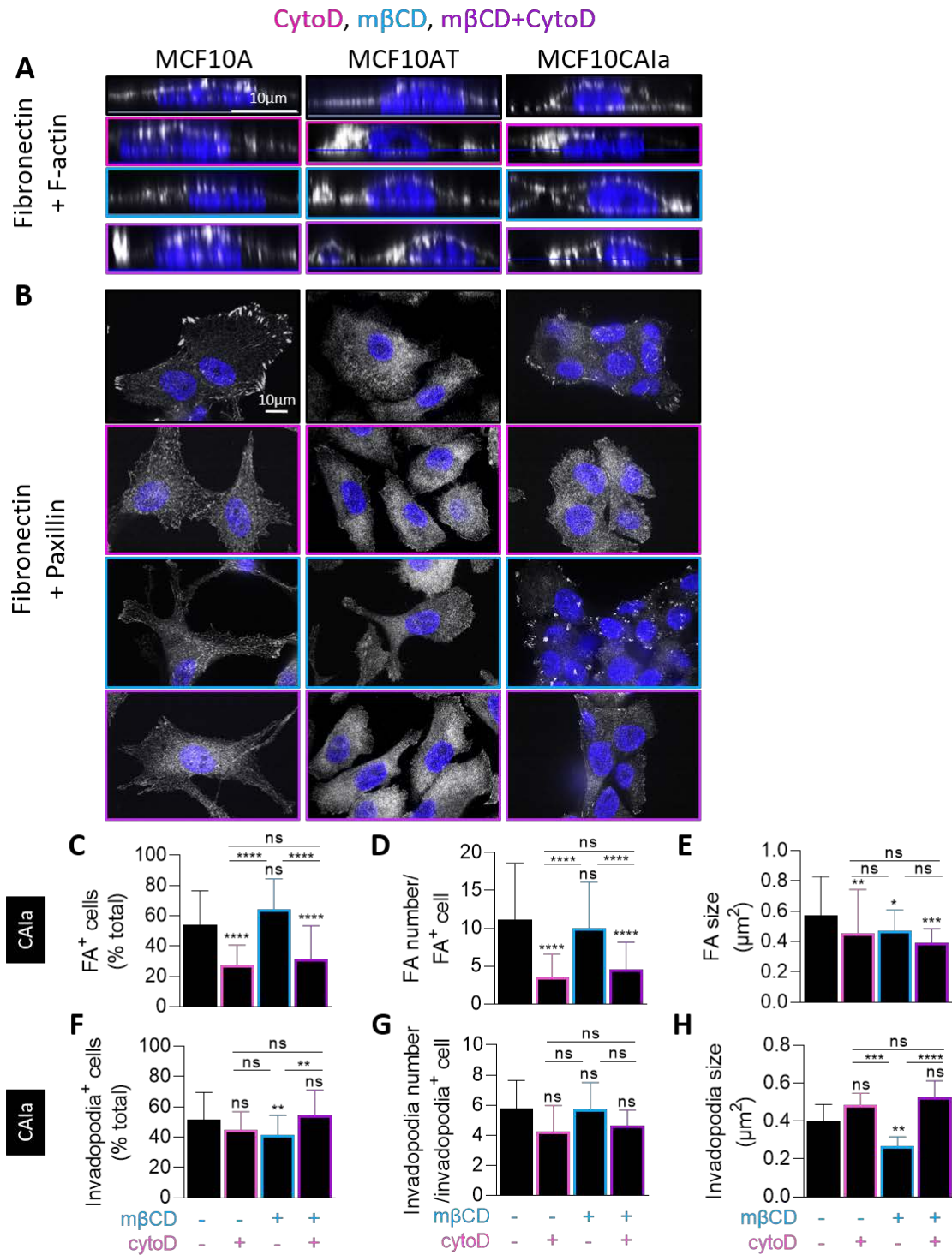


Fig. S11 Effect of combined cholesterol depletion and actin polymerization inhibition on actin cytoskeleton, focal adhesions and invadopodia in the MCF10A cell line series. Cell lines were treated with 2 mM mβCD (blue) in combination (purple) or not with 0.5 μM cytoD (pink) for 2h and then tested for confocal microscopy. (A) X-Z reconstructions of confocal images of the 3 cell lines plated on fibronectin-coated coverslips, treated or not with mβCD in combination with cytoD and then labeled with Phalloidin (F-actin) and nuclei (Hoechst). (B) Confocal images of the 3 cell lines plated on fibronectin-coated coverslips, treated or not with mβCD in combination with cytoD and immunolabeled with anti-Paxillin. Nuclei stained with Hoechst in blue. (C-H) Quantification of the

number of cells presenting focal adhesions (C), the number of focal adhesions per cell (D), the focal adhesion size (E; n=33-35 images [C] and n=33-84 cells [D,E] from 2-5 independent experiments), the number of cells presenting invadopodia (F), the number of invadopodia per cell (G) and the invadopodia size (H; n=8-65 images from 2 independent experiments) of CAIa plated on fibronectin-coated coverslips, treated with m β CD in combination or not with cytoD and immunolabeled with anti-Paxillin (C-E) or anti-Cortactin (F-H). One-Way ANOVA test followed by Tukey's comparison test (C-F) and Kruskal-Wallis test followed by Dunn's comparison test (G,H) ~~to compare all treatments~~

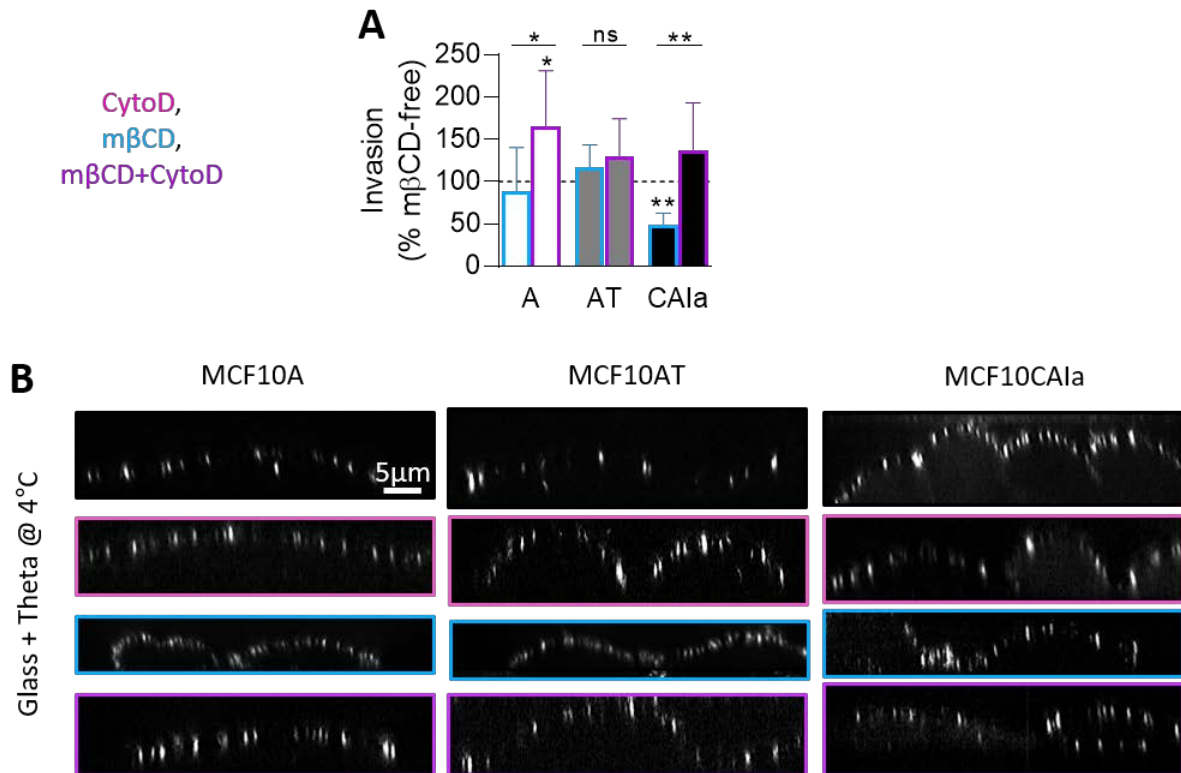


Fig. S12 Effect of combined cholesterol depletion and actin polymerization inhibition on invasion and surface cholesterol distribution in the MCF10A cell line series. Cell lines were treated with 2 mM mβCD (blue) in combination (purple) or not with 0.5 μM cytoD (pink) for 2h and then tested for invasion and confocal microscopy. (A) Quantification of invasion of the 3 cell lines in Transwell with a dense Matrigel layer toward 10% serum for 6-12h. Data are expressed in percentage of mβCD-free conditions (n=5-9 Transwell from 2-3 independent experiments). Mann-Whitney test ~~to compare mβCD vs mβCD + cytoD treatment~~ and Wilcoxon signed-rank test ~~to compare treatments with untreated CTL~~. (B) X-Z reconstructions of confocal images of the 3 cell lines plated on glass coverslips, treated or not with mβCD in combination with cytoD and then labeled at 4 °C with the mCherry-Theta toxin fragment

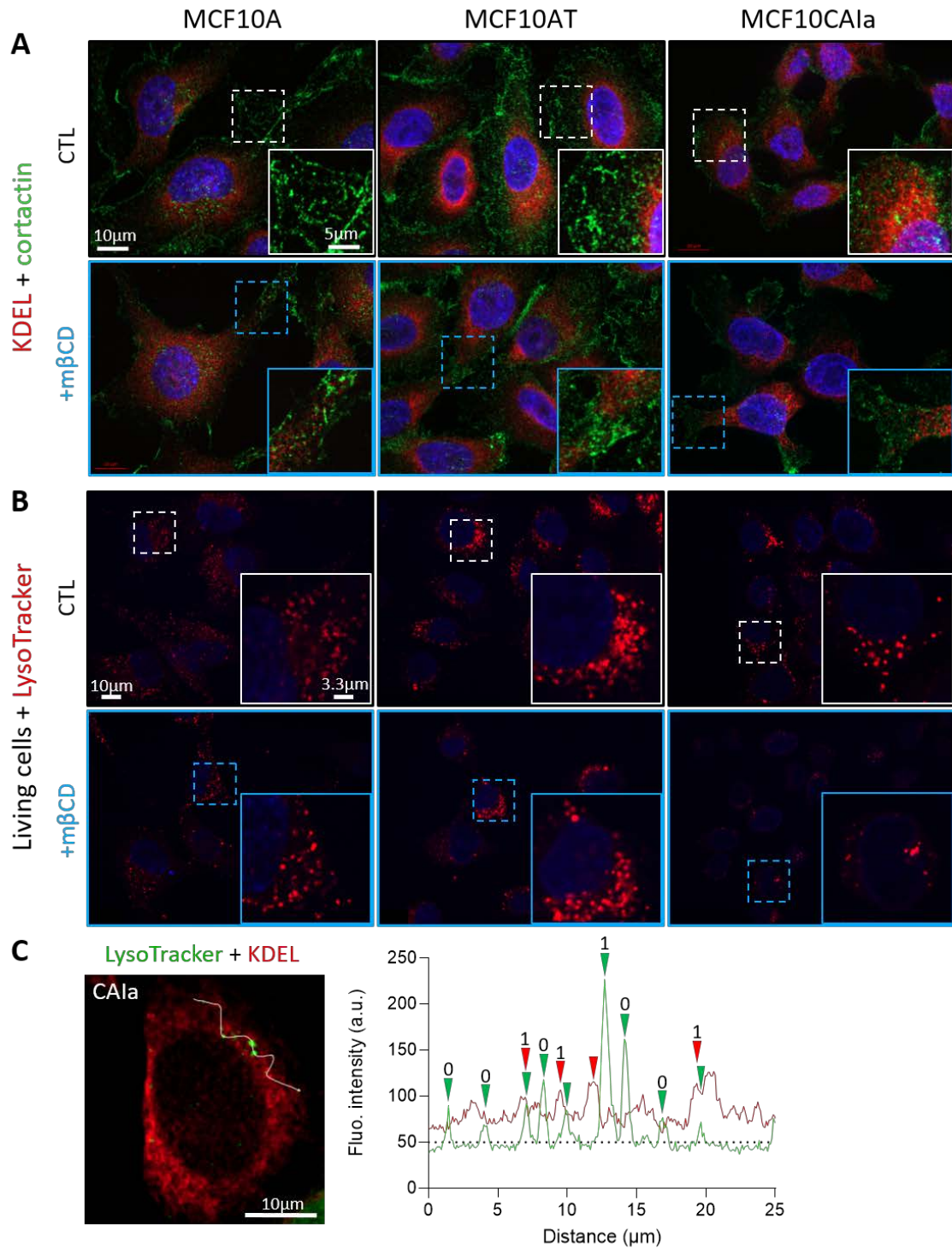


Fig. S13 Effect of cholesterol depletion on endoplasmic reticulum spreading towards the cell ventral side and lysosome distribution. The three cell lines were plated on fibronectin-coated coverslips, treated or not with 2 mM mβCD for 2h (blue) and then tested for confocal microscopy. (A) Coimmunolabeling with anti-KDEL (ER) and anti-Cortactin (to reveal invadopodia at the ventral side). (B) Labeling at 37 °C with the LysoTracker. Nuclei stained with Hoechst. Insets show ER network spreading near invadopodia sites (A) and lysosome abundance and distribution (B). (C) Representative fluorescence intensity profile along the line on the CA1a cell colabeled with anti-KDEL and the LysoTracker. Attribution of scores for close (=1) or loose (=0) contacts between green LysoTracker and red KDEL signals

References

1. Prausnitz MR, Lau BS, Milano CD, Conner S, Langer R, Weaver JC. A quantitative study of electroporation showing a plateau in net molecular transport. *Biophys J*. 1993;65(1):414-22. Epub 1993/07/01. doi: 10.1016/S0006-3495(93)81081-6. PubMed PMID: 7690262; PubMed Central PMCID: PMCPMC1225736.
2. Pollet H, Cloos AS, Stommen A, Vanderroost J, Conrard L, Paquot A, et al. Aberrant Membrane Composition and Biophysical Properties Impair Erythrocyte Morphology and Functionality in Elliptocytosis. *Biomolecules*. 2020;10(8). Epub 2020/08/06. doi: 10.3390/biom10081120. PubMed PMID: 32751168; PubMed Central PMCID: PMCPMC7465299.
3. Dumitru AC, Stommen A, Koehler M, Cloos AS, Yang J, Leclercqz A, et al. Probing PIEZO1 Localization upon Activation Using High-Resolution Atomic Force and Confocal Microscopy. *Nano Lett*. 2021;21(12):4950-8. Epub 2021/06/15. doi: 10.1021/acs.nanolett.1c00599. PubMed PMID: 34125553.
4. Dumitru AC, Mohammed D, Maja M, Yang J, Verstraeten S, Del Campo A, et al. Label-Free Imaging of Cholesterol Assemblies Reveals Hidden Nanomechanics of Breast Cancer Cells. *Adv Sci (Weinh)*. 2020;7(22):2002643. Epub 2020/11/27. doi: 10.1002/advs.202002643. PubMed PMID: 33240781; PubMed Central PMCID: PMCPMC7675049.
5. Carquin M, Conrard L, Pollet H, Van Der Smissen P, Cominelli A, Veiga-da-Cunha M, et al. Cholesterol segregates into submicrometric domains at the living erythrocyte membrane: evidence and regulation. *Cell Mol Life Sci*. 2015;72(23):4633-51. Epub 2015/06/17. doi: 10.1007/s00018-015-1951-x. PubMed PMID: 26077601.